Global ray tracing simulations of the SABER gravity wave climatology

Peter Preusse,[1] Stephen D. Eckermann,[2] Manfred Ern,[1] Jens Oberheide,[3] Richard H. Picard,[4] Raymond G. Roble,[5] Martin Riese,[1] James M. Russell III ,[6] and Martin G. Mlynczak[7]

Peter Preusse, Manfred Ern and Martin Riese, Institute of Chemistry and Dynamics of the Geosphere, ICG-1: Stratosphere, Research Center Juelich, Juelich, Germany. (p.preusse@fz-juelich.de)

S. D. Eckermann, Space Science Division, Code 7646, Naval Research Laboratory, Washington, DC 20375-5352, USA, (email stephen.eckermann@nrl.navy.mil)

Jens Oberheide, Department of Physics, Wuppertal University (BUGW), Gauss Str. 20, D-42097 Wuppertal, Germany

Richard H. Picard, Air Force Research Laboratory Battlespace Environment Division AFRL/VSBYB 29 Randolph Road Hanscom AFB, MA 01731-3010, USA

Raymond G. Roble, High Altitude Observatory, NCAR, National Center for Atmospheric Research, 3450 Mitchell Lane, Boulder, CO 80307, USA

James M. Russell III, Department of Physics Hampton University Hampton, VA 23668, USA

Martin G. Mlynczak, NASA Langley Research Center Hampton, VA 23681-0001, USA

[1]Institute of Chemistry and Dynamics of

Abstract. Since February 2002 the Sounding of the Atmosphere using Broadband Emission Radiometry (SABER) instrument on board the TIMED satellite has measured temperatures throughout the entire middle atmosphere. Employing the same techniques as previously used for the Cryogenic Infrared Spectrometers and Telescopes for the Atmosphere (CRISTA), we deduce from SABER V1.06 data five years of gravity wave (GW) temperature variances from 20 km to 100 km altitude. A typical annual cycle is presented by cal-

the Geosphere, ICG-1: Stratosphere,
Research Center Juelich, Juelich, Germany

[2]Space Science Division, Naval Research Laboratory, Washington, DC, USA

[3]Department of Physics, Wuppertal University (BUW),Wuppertal, Germany

[4]Air Force Research Laboratory, Hanscom Air Force Base, Hanscom, MA, USA

[5]High Altitude Observatory, National Center for Atmospheric Research, Boulder, CO, USA

[6]Hampton University, Hampton, VA, USA

[7]NASA Langley Research Center, Hampton, VA, USA

culating averages for the individual calendar months. Findings are consistent with previous results from various satellite missions. Based on July data and zonal mean GW momentum flux from CRISTA, a homogeneous and isotropic launch distribution for the Gravity wave Regional Or Global RAy Tracer (GROGRAT) is tuned. The launch distribution contains different phase speed mesoscale waves, some of very high phase speed and extremely low amplitudes, as well as waves with horizontal wavelengths of several thousand kilometers. Global maps for different seasons and altitudes as well as time series of zonal mean GW squared amplitudes based on this launch distribution match the observations well. Based on this realistic observation-tuned model run, we calculate quantities which cannot be measured directly and which are speculated to be major sources of uncertainty in current GW parameterization schemes. Two examples presented in this paper are the average cross-latitude propagation of GWs and the relative acceleration contributions provided by saturation and dissipation, on the one hand, and the horizontal refraction of GWs by horizontal gradients of the mean flow, on the other hand.

1. Introduction

Gravity waves (GWs) are an important dynamical driving force for the middle atmosphere. They are believed to be the main drivers of the mesospheric circulation and the cold summer mesopause [McLandress, 1998], to provide about half of the momentum required for driving the quasi-biennial oscillation (QBO) in the tropics [Dunkerton, 1997], and to contribute significantly to the Brewer-Dobson circulation [Alexander and Rosenlof, 2003]. However, GW parameterizations used in global modeling are highly simplified. In these schemes GWs are assumed to propagate purely vertically and remain inside the same general circulation model (GCM) grid column, not to change their horizontal propagation direction and to transfer momentum merely by wave-breaking processes [Hines, 1997; Warner and McIntyre, 1999; Alexander and Dunkerton, 1999; Medvedev and Klaassen, 2000] the latter themselves remaining a source of uncertainty [Chimonas, 1999; Hines, 1999; Fritts and Alexander, 2003; Achatz, 2007]. Furthermore, despite their importance experimental constraints on the global distribution of GWs and their sources remain poor.

Fetzer and Gille [1994] were the first to demonstrate that satellite remote sensors can resolve GWs. During the last decade the number of instruments with sufficient spatial resolution to observe GWs has increased. Each type of instrument can detect only a certain part of the full vertical and horizontal wavenumber spectrum of GWs. Overviews and comparisons of different observation methods as well as the range of detectable vertical and horizontal wavelengths are given by Wu et al. [2006] and Preusse et al. [2008]. Infrared emission limb sounders have the advantage that they can resolve a wide range of vertical wavelengths. A particular benefit of the limb temperature retrievals from the

Sounding of the Atmosphere using Broadband Emission Radiometry (SABER) instrument on the TIMED satellite [Mlynczak, 1997; Russell et al., 1999; Yee et al., 2003; Remsberg et al., 2008] is that these measurements cover the entire middle atmosphere and lower thermosphere.

The SABER instrument has now operated for more than six years. This provides the opportunity to search for semi-annual, annual and biennial variations of GW amplitudes [Krebsbach and Preusse, 2007; Ern et al., 2008] and to generate a statistically meaningful climatology of the annual cycle. This distinguishes SABER from previous GW investigations of infrared limb emissions (e.g. Fetzer and Gille [1994]; Eckermann and Preusse [1999]; Preusse and Ern [2005]; Ern et al. [2006]), which cover a smaller altitude range and discuss (with the exception of the CLAES data; Preusse and Ern [2005]) only selected time slices of one month or less.

The SABER time series of GW temperature variances offers more comprehensive test conditions for global GW modeling, and in particular, provides the opportunity to adapt the launch setup of a model according to measured data.

Conventionally, global GW modeling starts with a semi-empirical or process-based GW source distribution, propagates the waves through the background wind and temperature fields and compares the results to measured distributions. For instance, Eckermann [1992] performed ray tracing simulations based on a launch distribution containing three horizontal wavelengths (200 km, 400 km and 800 km), four phase speeds (0 ms^{-1}, 5 ms^{-1}, 15 ms^{-1} and 35 ms^{-1}) and eight azimuthal directions. The results were semi-quantitatively compared to previous results from stratospheric sounding rockets in terms of annual cycle and preferrential propagation direction. Alexander [1998] used a model based on a compre-

hensive set of single waves with horizontal wavelengths between 6 km and 800 km, periods between 15 minutes and 4 hours, and constant launch momentum flux for all waves, which implies a "red" distribution of GW-induced temperature variance as a function of horizontal wavenumber. The results were compared to Microwave Limb Sounder (MLS) [Wu and Waters, 1997] and in-situ measurements [Eckermann et al., 1995; Allen and Vincent, 1995]. Eckermann and Preusse [1999] and Jiang et al. [2002, 2004b] used the physics-based launch distribution of the Naval Research Laboratory Mountain Wave Forecast Model (NRL-MWFM) and compared GW hindcasts to measurements by the CRyogenic Infrared Spectrometers and Telescopes for the Atmosphere (CRISTA) infrared emission limb sounder and to MLS data, respectively. Though in both cases the measurements were matched by the model hindcasts inside the range of uncertainty, Jiang et al. [2004b] concluded that there were still too many degrees of freedom to infer model improvements or identify model deficiencies. Alexander and Rosenlof [2003] vary four tunable parameters of a horizontal phase speed spectrum and infer most-likely values for the tropics by maximizing correlation coefficients between GW-modeling results and GW-drag inferred from a combination of data assimilation and satellite observations. Ern et al. [2006] compared model results from the CRISTA-1 and CRISTA-2 missions with offline simulations using the Warner and McIntyre spectral parameterization scheme [Warner and McIntyre, 1999, 2001]. They were able to confine the ranges of the tunable model parameters, but also found indications that even with the best choice of parameters the model overestimates GW activity at high summer latitudes. A ray tracing simulation consisting of four mid-frequency and three long horizontal wavelength components for August 1997 com-

pared to CRISTA-2 and SABER GW squared amplitudes [Preusse et al., 2006] seems to confirm this finding but covers too small a latitude range to be conclusive.

In this paper we take the opposite approach. We compare the modeled results for single spectral components (i.e. GWs of one horizontal wavelength, phase speed and amplitude at launch, cf. section 3.2) with the SABER measurements and select components for a composite experiment in such a way that zonal mean GW squared amplitudes for July well match the SABER observations. Further constraints are deduced from CRISTA momentum flux estimates. In this way we determine an "optimal" launch distribution. The comparison of global maps for different months and altitudes as well as the comparison of the annual cycle provide an independent test-base and confirm the choice of single spectral components and their relative contribution to the composite experiment. Although there remain uncertainties in the composition of the spectrum, such a measurement-guided GW model setup can be valuable for quantitatively estimating the importance of effects conventionally neglected in GW parameterization schemes, such as oblique wave propagation, refraction of the horizontal wave vector and wave damping by infrared radiation and background turbulence. These simplifications are sources of uncertainty in GCMs with parameterized GW drag [Watanabe, 2008].

For instance, Bühler and McIntyre [2003] made the point that the horizontal refraction of GWs by strong horizontally-sheared winds near the edge of the polar vortex acts at different locations and in a different way than is predicted by conventional GW drag parameteizations. Their approach, however, is purely theoretical and therefore cannot quantitatively assess the importance of horizontal refraction in the real world. Recently, Hasha et al. [2008] have studied the impact on orographic GW drag parameterization

in the troposphere and lower stratosphere for more realistic wind profiles. Gravity wave induced mean wind forcings calculated in this paper will provide a first realistic estimate of the overall impact of this effect.

The technique for extracting GW signals from SABER temperature profiles is described in section 2. Section 3 introduces the Gravity wave Regional Or Global RAy Tracer (GROGRAT) and the background atmosphere used for the ray tracing experiments. The "optimal" launch distribution of GWs is inferred in section 4. In section 5, global maps as well as zonal mean cross sections of a typical annual cycle composed from almost five years of SABER data are compared to GROGRAT modeling results based on this launch distribution. In Section 6 the GROGRAT model results are used to estimate average cross-latitude propagation and GW-induced mean-flow accelerations. A summary and discussion are given in section 7.

2. Instrument and analysis technique

The SABER instrument [Mlynczak, 1997; Russell et al., 1999; Yee et al., 2003] is an infrared emission limb sounder covering the upper troposphere, stratosphere, mesosphere and lower thermosphere. In this paper we use temperatures from version 1.06 (V1.06) retrievals. Temperatures are retrieved from the main CO_2 ν_2 emission at 15 μm. A coupled retrieval algorithm evaluates CO_2 densities and temperatures simultaneously from 4.3 μm and 15 μm emissions and takes into account non-local thermodynamic equilibrium (NLTE) effects [Mertens et al., 2001, 2004]. NLTE effects and interaction with chemistry start to exert an influence above $\sim$70 km altitude and become increasingly important in the mesopause and lower thermosphere region [Kutepov et al, 2006]. Accordingly, SABER temperature errors are 1-2 K for altitudes below 80 km, and increase above this altitude

[Mertens et al., 2001; Remsberg et al., 2008]. The most recent estimate [Remsberg et al., 2008] for V1.07 states a preliminary absolute temperature error of 3 K and a noise error of 1.2 K at 85 km altitude. In addition, a second particularly difficult region to retrieve is the tropical tropopause, because measurements below it are likely to be cloud contaminated and because of the very sharp knee in tropopause temperatures.

The TIMED satellite performs six yaw maneuvers per year, changing from a south-looking (83°S–52°N) to a north-looking (52°S–83°N) geometry and vice versa. The relative times of the yaw maneuvers during the year are the same for different years, so that, for instance, SABER always views to the south in August.

SABER temperatures between 20 and 100 km altititude are analyzed employing the algorithms described by Preusse et al. [2002]. The global background atmosphere is estimated by a zonal wavenumber 0–6 Kalman filter and subtracted from the individual profiles. This horizontal scale separation approach preserves the vertical spectral information on GWs in the data. Horizontal wavelengths range between the visibility limit of 100-200 km [Preusse et al., 2002] and zonal wavenumber 7. The upper wavelength limit, however, is probably not a serious constraint, since horizontal wavelength estimates from CRISTA [Preusse et al., 2006] indicate that the upper end of the horizontal wavelength distributions is limited by physical processes rather than by the analysis method.

After separation from the background atmosphere, the residual temperature profiles are analyzed by a combination of maximum entropy method (MEM) and harmonic analysis (HA), thus providing the amplitudes, vertical wavelengths and phases of the two strongest wave components at each altitude of a measured profile [Preusse et al., 2002]. The width of the sliding vertical window of the harmonic analysis is 10 km.

In this paper, we focus on seasonal variations which are persistent for different years. We therefore bin the data according to calendar months for the almost five-year time series from February 2002 to December 2006, so that, for instance, July values contain data from July 2002, 2003, 2004, 2005 and 2006.

3. Global gravity wave model

3.1. Description of the ray tracer

The observed GW distributions are compared to results from global GW ray tracing experiments using the Gravity wave Regional Or Global RAy Tracer (GROGRAT). A full description of the GROGRAT model can be found in Marks and Eckermann [1995] and Eckermann and Marks [1997] and we here give a brief summary only. GROGRAT is based on the non-hydrostatic, rotational GW dispersion relation

$$\hat{\omega}^2 = \frac{N^2(k^2+l^2) + f^2(m^2 + \frac{1}{4H^2})}{k^2 + l^2 + m^2 + \frac{1}{4H^2}}, \quad (1)$$

where $\hat{\omega}$ is the intrinsic frequency, N is the buoyancy frequency, k, l and m are the wavenumbers in x, y and z directions, repectively, and H is the density scale height. The ray tracing equations take into account refraction of the wave vector due to vertical as well as horizontal wind gradients and meridional gradients of the Coriolis force. Amplitudes are calculated according to wave action conservation. In addition, dissipative processes such as radiative and turbulent damping, which affect waves with amplitudes well below any saturation threshold for wave breaking, are parameterized.

3.2. Setup of the model experiment

The representativeness of a ray tracing experiment largely depends on the choice of the background atmosphere. In the present study, we use European Centre for Medium Range Weather Forecasts (ECMWF) reanalyses from 0–50 km altitude and winds and temperatures from the Thermosphere Ionosphere Mesosphere Energetics General Circulation Model (TIME-GCM) [Roble and Ridley, 1994] from 40–100 km altitude, with the two smoothly blended in the overlap region from 40-50 km altitude following Preusse et al. [2008]. ECMWF reanalysis data are used in numerous scientific studies and capture the synoptic scale features of the troposphere and stratosphere well [Borsche et al., 2007; Ern et al., 2008]. For altitudes above the stratopause, data from a TIME-GCM experiment conducted especially for the TIMED mission are used. In order to reproduce the actual atmospheric state, the TIME-GCM is nudged at 30 km altitude to NCEP reanalyses and radiation-forced migrating tidal components at the lower boundary are provided from the GSWM tidal model [Hagan et al., 1995]. The GCM was run continuously from January 2002 to December 2004 and has been used, for example to analyze tides [Oberheide et al., 2006]. Combining ECMWF and TIME-GCM data, we therefore generate a background atmosphere representing the actual conditions at the time of the SABER observations to the best of our knowledge.

For the ray-tracing model runs, the background atmosphere winds and temperatures are interpolated to a regular grid with a resolution of 2.5° latitude and 3.75° longitude on 41 pressure levels corresponding to an altitude spacing of 2.5 km. Latitudes range from 85 S to 85 N (GROGRAT does not propagate rays across the pole).

The initial launch conditions for the waves follow the the same overall approach used by Preusse et al. [2006] in their GROGRAT–SABER comparison study. A wave is initialized

at it's launch latitude, longitude and altitude with a specific propagation direction, horizontal wavelength, phase speed and amplitude. In order to perform a systematic analysis we launched waves homogeneously and isotropically on a regular grid of 20° longitude × 5° latitude in eight equispaced azimuth directions, i.e. every 45° starting from due east. Such a "single spectral component experiment" (SCE) is defined by the GW horizontal wavelength λ_h, ground-based phase speed c_h, peak horizontal wind amplitude $\hat{u}_l$ at launch level and launch altitude. (Note that SABER measures temperatures, but launch amplitudes for GROGRAT are specified in terms of wind.) Combining several SCEs, we can emulate a full launch spectrum.

An example of an SCE launch grid is given in Figure 1. The launch locations are indicated by black asterisks. At each launch location rays are launched into eight azimuth directions. Resulting ray-paths for waves launched at the zero meridian are shown. The color indicates altitude. Waves propagating against the wind attain large vertical group velocities and quickly reach the mesosphere, whereas waves propagating with the wind "drift" large distances downstream in taking much longer to propagate verticall.

Guided by previous global GW modeling studies as well as studies of GWs in a GCM [Alexander, 1998; Manzini and McFarlane, 1998; Ern et al., 2004, 2006] we chose a launch altitude of 5 km for all SCEs. Due to computational costs, we were forced to restrict the number of SCEs. An overview of all SCEs which we have considered is given in Table 1. We therefore launch only horizontal wavelengths which match the observational filter of SABER and in particular do not launch short horizontal wavelength waves. As discussed in some depth by Preusse et al. [2006], we know from previous studies that a combination of medium and long horizontal wavelength waves is required. We mimic this by using

only two medium-scale horizontal wavelengths covering the full range of phase speeds and only three phase speeds with longer horizontal wavelengths. In particular, only for $c_h = 30$ ms^{-1} do we use a representative set of horizontal wavelengths from the medium-scale to very long (λ_h =6000 km). In order to determine the shape of the spectrum, we launch some SCEs which are discerned only by their amplitudes, but are equal in horizontal wavelength λ_h and phase speed c_h (e.g. SCEs 7 and 9; 13 and 15). This is necessary, since GWs interact nonlinearly with the background atmosphere. In particular, the launch amplitude determines the saturation altitude. We will discuss this in detail in the following section. Using intermittency factors, we can adapt the contribution of single SCEs to the total GW variance or momentum flux in order to match the observed distribution (see section 4).

4. Selection of a launch distribution

4.1. Intermittency or weighting factors

Intermittency factors were introduced into GW parameterization schemes in order to adjust the resulting GW forcing of the mean background winds to the needs of the GCM [Holton, 1982; Alexander and Dunkerton, 1999; Fritts and Alexander, 2003]. They can be thought of as describing that GWs are intermittent in their nature and therefore not always present in the atmosphere or incompletely fill a given grid box. In this paper, we compose the spectrum of waves from single SCEs with different phase speeds and amplitudes, but always the same number of rays. In order to weight the different SCEs we introduce weighting or intermittency factors when calculating averages (e.g. zonal mean squared amplitudes). Every ray present in a considered volume (e.g. a latitude-altitude bin) is weighted by the intermittency factor of the respective SCE. This again

can be thought of as describing the fact that some GWs (some SCEs) might be present more frequently or cover larger areas. Since in this paper we calculate average values the absolute value of the intermittency factor has no physical significance and only the relative distribution among the different SCEs influences the result.

4.2. Characteristics of single SCEs

The launch spectrum is generated from individual SCEs with respective intermittency factors in an iterative tuning process. In a first step zonal mean squared amplitudes for July from single SCEs are compared to the SABER measurements. Salient features in the distributions motivate the general composition and a first guess of suitable intermittency factors. This is described in this subsection. In a second step we vary these initial intermittency factors until the resulting composite agrees with the SABER measurements. This is discussed in subsection 4.3. We have chose July for tuning, since July distributions have a large summer-winter asymmetry. Since the southern polar vortex is stable (except in 2002), a single-day GROGRAT experiment for 15 July is sufficiently representative for tuning the wave components. Time series of the typical annual cycle discussed in section 5 then provide an independent test of the chosen launch distribution.

Figure 2 compares zonal mean GW squared amplitudes for vertical wavelengths between 5 and 50 km measured by SABER (panel b) to zonal mean winds (panel a) and to the zonal means from single SCEs (panels c-i). The zonal mean zonal winds are ECMWF-TIME-GCM composites for 15 July 2003, i.e. the zonal mean of the three-dimensional global wind field used for the GROGRAT simulations. Details of the SCE launch parameters for the results shown in panels c-i are given in Table 1 together with further SCEs discussed below. For historical reasons, launch amplitudes are specified in GROGRAT as wind

amplitudes in ms^{-1}. For all results shown we use squared temperature amplitudes in K^2, plotted in dB relative to 1 K^2.

To assess the temperature perturbations induced by a single SCE in a certain region or in a zonal mean we need to consider the number of rays in this region as well as the amplitude of the rays. In calculating zonal means we therefore average over the ray amplitudes of the considered SCE as well as a constant number of 0.05 K on a horizontal grid of 2.5° latitude and 5.0° longitude serving as a background. In this way there are as many background values as rays launched. If, for instance, very few rays can propagate to a certain latitude or altitude, the mean value for this latitude or altitude will be close to the background (i.e. very low), and if all launched rays reach a certain latitude or altitude the mean value will be the average of the background value and the average amplitude in this region. The latter emulates that in the composite experiments there is allways a mixture of different SCEs contributing to the average. A detailed motivation and discussion of the background is given in section 4.2 of Preusse et al. [2006]. The GROGRAT distributions shown in Figure 2 contain only data where the vertical wavelength is between 5 and 50 km and the horizontal wavelength is longer than 100 km in order to mimic the instrument visibility filter for SABER (cf. Preusse et al. [2002, 2006]).

The salient features of the measured distribution in panel b) are a general increase in GW squared amplitudes from low to high altitudes, and high values associated with strong winds (cf. panel a) in the southern polar vortex and in the northern subtropics. For the subtropical maximum, convective forcing is an important source [Preusse et al., 2001; Jiang et al., 2004a; Preusse and Ern, 2005]. At low altitudes (below 25 km) a tropical maximum is found, which extends from about 10° S to the northern subtropics.

It presumably consists of long horizontal wavelength, low frequency GWs, which can only exist around the equator because their frequencies are below the Coriolis parameter limit at higher latitudes [Alexander et al., 2002; Ern et al., 2004; Preusse et al., 2006]. These structures are discussed in more detail below.

There is one major difference between the new data shown in Figure 2 and that of the previous investigation by Preusse et al. [2006]. The new data exhibit a strong and monotonic increase of GW squared amplitudes above 80 km in contrast to Figure 2 in Preusse et al. [2006], which shows a decrease of amplitude on top of the southern polar vortex. The earlier investigation was based on a previous version of the SABER temperature retrievals (Version 1.04) and focuses on waves with vertical wavelengths between 5 and 25 km. Close investigation of Version 1.04 data shows that above 65 km altitude the temperature profiles appear artificially smooth and that short vertical wavelengths are filtered out completely. The new Version 1.06 data studied in the current paper do not exhibit this artifical smoothing. In addition, here we consider a wider vertical wavelength range (5-50 km). Both effects contribute to the difference. Version 1.06 data analyzed for 5-25 km vertical wavelengths (not shown) exhibit a local maximum associated with the southern polar vortex and a slight decrease directly above (at ∼60-70 km). However, above 85 km we find a monotonic strong increase in GW squared amplitudes for the shorter vertical wavelength GWs, similar to the increase observed in Figure 2b.

The effects of wind filtering and the correlation with background wind fields is strongest for the slow waves, for instance SCE 1 shown in Figure 2c. The strong latitudinal gradients observed in this panel are caused by three mechanisms, described in more detail by Preusse et al. [2006]. First, the waves are much slower than typical wind velocities in

311 the stratosphere and the waves are therefore frequently subjected to critical level filtering
312 when the ground-based horizontal phase speed c_h matches the background wind velocity
313 U in the direction of the wave vector ($c_h = U$). Second, the vertical wavelength is re-
314 fracted by the background winds according to the approximate hydrostatic irrotational
315 GW relation

$$\lambda_z = 2\pi \frac{|c_h - U|}{N} \tag{2}$$

316 where λ_z is the vertical wavelength and N is the buoyancy frequency. (Equation 2 is
317 valid in the mid-frequency approximation $f^2 \ll \hat{\omega}^2 \ll N^2$.) Since N is about 0.02 s^{-1}
318 in the stratosphere, a 5 km lower limit of the vertical wavelength visibility filter (i.e.
319 the shortest vertical wavelength observable by SABER) corresponds to an intrinsic phase
320 speed $|\hat{c}| = |c_h - U|$ of 16 ms^{-1}, which is much faster than the ground-based phase speed
321 of these waves. These waves are thus only visible to SABER (and hence only appear
322 in Figure 2), if they are refracted favorably by the background winds to large intrinsic
323 phase speeds. This "visibility effect" was introduced by Alexander [1998]. Third, due
324 to decreasing density waves grow in amplitude with increasing altitude. However, the
325 maximum amplitude is limited by stability (saturation) criteria. If we assume convective
326 instability to be the limiting process, the maximum temperature amplitude $\hat{T}_{max}$ of a wave
327 before breaking is related to the vertical wavelength by

$$\hat{T}_{max} = \frac{N^2 \overline{T}}{2\pi g} \lambda_z \tag{3}$$

with $\overline{T}$ the background temperature and g Earth's gravitational acceleration. Waves propagating against the background wind attain larger vertical wavelengths and hence can have larger amplitudes.

For the faster waves shown in the lower three rows of Figure 2, the lower limit of the visibility filter ($\lambda_z \geq 5$ km) is sufficiently short to retain most of the waves regardless of the background winds, and visibility effects are therefore less important for the distributions shown in panels d–i. For these SCEs, local maxima and horizontal structures are determined by the wave saturation amplitude and by whether the waves have achieved sufficient amplitudes to become saturated or not. The latter is the difference between panels d and e as well as f and g, respectively. The two SCEs shown in the left row are launched with higher amplitudes $\hat{u}_l$ than their counterparts in the right row. They start to saturate at altitudes of ∼50 km (panel d) and ∼70 km (panel f). Only above the saturation altitude do GW squared amplitudes form local maxima related to high wind velocities, and on top of the mesospheric jets the GW squared amplitudes decrease. In contrast, the waves shown in panel g (right column) never reach the saturation limit and steadily grow in amplitude with altitude.

The steady increase of GW squared amplitudes observed in the SABER data (panel b) at high altitudes is therefore an indication of the dominance of fast waves at high altitudes (>80 km). On the other hand, the low wave activity in the summer high latitudes at lower altitudes can only be matched by an SCE with a high saturation altitude and hence a low launch amplitude. The launch amplitudes given in Table 1 therefore demonstrate that if these waves originate in the troposphere or lower stratosphere (TLS) they could hardly be detected close to their source altitude by any measurement technique because of their

very low amplitudes. On the other hand, this means that there is a good likelihood of such waves being forced by background fluctuations.

Figure 2i shows long horizontal wavelength waves. Their ground-based frequency $\omega_{gb} = 2\pi c_h / lambda_h$ is lower than the Coriolis parameter $|f|$ at most latitudes. Compared to a phase speed of 30 ms^{-1} tropospheric wind speeds are, in genaral, too low to induce substantial Doppler shift and therefore at low altitudes these waves can only occur around the equator. At higher altitudes they can escape this confinement if they propagate opposite to strong background winds and therefore attain higher intrinsic frequencies. Long horizontal wavelength waves are therefore likely responsible for the tropical maximum observed in Figure 2b as well as in a number of previous in situ and satellite observations [Alexander et al., 2002; Ern et al., 2004; Preusse et al., 2006].

Fast waves of long horizontal wavelengths shown in Figure 2h are not strictly prohibited by the dispersion relation at higher latitudes, but are more likely subject to wave damping and critical level filtering than their shorter wavelength counterparts (e.g. the SCEs shown in panels f and g). Since they are also able to propagate far away from their sources, such waves can best match the slanted isolines of the SABER observations at mid and high northern latitudes (between 30°N and 70°N the isolines in Figure 2b have a slope close to 45°).

4.3. Choice of the intermittency factors

The comparison of single SCEs with the measurements in Figure 2 gives us a general guidance for composing a launch "spectrum" from a number of SCEs. Additional constraints can be gained from high vertical resolution observations of a universal spectrum of GWs [Fritts, 1984; Tsuda and Hocke, 2002; Fritts and Alexander, 2003] indicating that

GWs with vertical wavelengths shorter than 2-4 km in the stratosphere are saturated. In addition, horizontal wavelength and momentum flux distributions from CRISTA [Ern et al., 2004, 2006], which had twice as dense horizontal sampling as SABER, can give further guidance [Preusse et al., 2006].

We now generate composites from the single SCEs guided by the comparison in subsection 4.2. Different composites are generated by varying the intermittency factors (IMFs). For each altitude and geographical bin defined by its latitude (and in case of maps longitude) boundaries the single wave events are weighted by the IMFs when calculating an average. Some examples of different composites are given in Figure 3. Figure 3a and b repeat the zonal wind and the SABER zonal mean cross section from Figure 2a and b, panels c-g show five different experiments with IMFs as listed in Table 1.

Figure 3c uses the same intermittency factors as the earlier experiment described by Preusse et al. [2006] and can be considered as a control run. However, despite equal IMFs there are differences between the setup used by Preusse et al. [2006] and the setup of the results shown here. First, the earlier experiment was for August 1997 whereas here we use wind data for July 2003. Second, the earlier experiment was based on a combination of ECMWF data and CRISTA geostrophic winds whereas the new one is based on ECMWF data and TIME-GCM simulations for the higher altitudes and thus covers a wider latitude range. Finally here we use a wider vertical wavelength filter for the new results shown in Figure 3. Figure 8 a-d of Preusse et al. [2006] therefore shows similar (note the different color scales), but not identical results to those in Figure 3c.

The main shortcoming of the earlier composition chosen by Preusse et al. [2006] is the overestimation of GW squared amplitudes at the high summer latitudes. In addition,

after the change from SABER Version 1.04 to 1.06 data and by taking into account longer vertical wavelengths we observe a monotonic increase of GW squared amplitudes at high altitudes. These two aspects motivated us to modify the original wave-source settings of Preusse et al. [2006]. We removed the contribution of fast waves launched with moderate, unsaturated amplitudes (SCEs 7 and 13) and replaced them by fast waves launched with very small amplitudes (SCEs 9 and 15). This composite Exp04 is shown in Figure 3d. The composite is improved in that it does not greatly overestimate the high latitude summer values, but has the side effect of underestimating the GW squared amplitudes between 30°S and the equator. In addition, this modification does not improve the agreement between measurement and modeling at high altitudes above 80 km.

To match both relatively high values at the equator and the gradual spread of GW variances towards high summer latitudes (c.f. isolines tilted about 45° between 20N and 80N in Figures 2b and 3b), we introduced a component with long horizontal wavelength and fast phase speed (SCE 23, Figure 2h). In addition, there is an identical SCE differing only in the launch amplitude (SCE 22, not shown).

Experiments 14, 32 and 232 (panels e-g) introduce these new SCEs using different sets of intermittency factors (IMFs). Experiment 32 and 232 differ in the horizontal wavelengths of the mesoscale waves, i.e. SCEs 2, 4, ... 18 with 500 km horizontal wavelength each replace SCEs 1, 3, ... 17 with 200 km horizontal wavelength, respectively.

As the experiment numbers indicate, the choice of the "optimal" composite is based on a trial and error procedure of varying the intermittency factors until the best overall agreement is found with the observations. However, Figure 3 shows that experiments 32 and 232 are almost indistinguishable in terms of GW squared amplitudes. Therefore

we need additional data to constrain the horizontal wavelength, so we compare absolute values of momentum flux from the ray tracing experiments to CRISTA momentum flux estimates.

4.4. Horizontal wavelength and momentum flux constraints

CRISTA took measurements during two one-week periods in October 1994 (CRISTA-1) and August 1997 (CRISTA-2) [Offermann et al., 1999; Riese et al., 1999; Grossmann et al., 2002]. Both missions have been analyzed for absolute values of GW momentum flux [Ern et al., 2006]. The inferred momentum flux values well agree with measurements from long-duration balloons over Antarctica [Hertzog et al., 2008].

Momentum flux can be inferred from temperature variations by equation (7) of Ern et al. [2004] if both the horizontal wavelength and the vertical wavelength of the wave are known :

$$|F_{ph}| = \frac{1}{2}\rho \left|\frac{k_h}{m}\right| \left(\frac{g}{N}\right)^2 \left(\frac{\hat{T}}{T}\right)^2 \tag{4}$$

where $k_h = 2\pi/\lambda_h$ is the horizontal wavenumber, $m = 2\pi/\lambda_z$ is the vertical wavenumber, $\hat{T}$ is the temperature amplitude, and ρ, N and T are density, buoyancy frequency and temperature of the background atmosphere. The horizontal sampling distance of CRISTA was $\sim$200 km, which implies a Nyquist wavelength (i.e. shortest resolvable wavelength) of 400 km. Ern et al. [2004] showed that CRISTA data undersample the measured GWs and that some effects of aliasing occur when inferring horizontal wavelength distributions. The horizontal sampling distance of SABER is twice as large as the CRISTA sampling

distance and therefore too coarse to retrieve horizontal wavelengths and thus momentum flux estimates for GWs.

Figure 4 compares absolute values of GW momentum flux in dB relative to 1 Pa measured by CRISTA-2 (Aug. 1997, panel a) and CRISTA-1 (Nov. 1994, panel e) with GROGRAT results for Exp. 32 (b, f), Exp. 132 (c, g) and Exp. 232 (d, h) calculated for 15 Aug. 2003 (b-d) and 15 Nov. 2003 (f-h). The difference among the three composites is the horizontal wavelength distribution. Experiment 32 uses λ_h =200 km for all mesoscale components, Exp. 132 uses λ_h =200 km for the fast waves and λ_h =500 km for the slow waves, which dominate the lower altitudes, and Exp. 232 uses λ_h =500 km for all mesoscale components. An observational filter of $\lambda_z = [5, 20]$ km is applied to the GROGRAT results. Note that due to the observational filter GW momentum flux can increase with increasing altitude. This is observed, for instance, at the summer polar mesopause. Although the momentum flux of each individual wave remains constant or decreases with altitude icreases with height are possible because some waves carrying large GW momentum flux are refracted in vertical wavelengths, shift into the range of the observational filter, and become visible in the zonal means.

From (4) we expect the 500 km horizontal wavelength waves to carry a fraction of 2/5 of the momentum flux of the 200 km waves, which corresponds to an offset of $\sim$4 dB in Figure 4. In agreement with Preusse et al. [2006], we find that momentum flux distributions based on a typical wavelength of 500 km for the mesoscale waves match the observations well, whereas assuming a typical wavelength of 200 km overestimates the GW momentum flux. Experiment 132, which combines 500 km horizontal wavelength for the slower and 200 km horizontal wavelength for the faster mesoscale SCEs (cf. Table 1), is very simi-

lar to Exp. 232 in the stratosphere. This means that the horizontal wavelengths of the very fast waves with small launch amplitudes cannot be sufficiently constrained by the CRISTA stratospheric observations.

Overall, given both GW squared amplitudes and momentum flux, Exp. 232 matches the observations best. GW squared amplitudes show low values in the summer hemisphere and tilted isolines at a similar angle as the observations, reasonably high values at the equator and a monotonic increase in the upper mesosphere. The momentum flux values compare favourable with the CRISTA measurements. We therefore choose Exp. 232 for further discussion.

5. The annual cycle in SABER and GROGRAT GW results

5.1. Global maps in the lower stratosphere

SABER:

Figure 5 shows global maps at 28 km altitude of GW squared temperature amplitudes of the largest amplitude wave component for vertical wavelengths between 5 km and 50 km. The data are binned to a 1° latitude × 2° longitude grid using a triangular weight of 800 km width, i.e., a SABER point is weighted 1 if it coincides with a grid point, weighted zero if the distance between SABER point and grid point is larger than 800 km, and weighted with a linearly interpolated value between 0 and 1 for distances in between.

The resulting maps for the two solstices (January and July) are essentially mirror images with respect to the equator and are both very different from the two maps at equinox (April and October). At the solstices a very pronounced winter vortex maximum is the dominant feature and a secondary maximum can be found in the tropics and subtropics of the summer hemisphere. The GW variances at high summer latitudes are very low. These

481 are all features well known from GW temperature variances extracted from a number of
482 different satellite instruments [Wu and Waters, 1997; Ern et al., 2004, 2006; de la Torre
483 et al., 2006; Wu and Eckermann, 2008]. The summer low latitude maximum is commonly
484 attributed to convectively generated GWs in the monsoon regions and above high sea
485 surface temperature regions and correlates well with convection proxies [McLandress et
486 al., 2000; Preusse et al., 2001; Jiang et al., 2004a; Preusse and Ern, 2005]. The comparison
487 of July and August values shows that the most active region in Asia shifts eastward from
488 the Indian monsoon towards the Kuro-Shio ocean stream. This more eastward position of
489 subtropical wave activity is very similar to the CRISTA observations [Preusse et al., 2001;
490 Ern et al., 2004] and is connected with a further northward shift into the subtropics.
491 It should also be noted that high GW momentum flux in the summer subtropics was
492 explained, at least to some extent, by wind filtering [Ern et al., 2004].

493 There are two noticeable differences between the two respective hemispheres. First,
494 during solstices the wave activity in the winter vortex is stronger and much more zonally
495 symmetric in the southern hemisphere (SH) due to a more stable winter polar vortex.
496 Second, the subtropical band of high wave activity extends further northward in July
497 than southward in January, which might be due to a more pronounced monsoon season
498 in the northern hemisphere (NH).

499 At the equinoxes, tropical GW variances are symmetric about the equator and much
500 less pronounced than at the solstices. At higher latitudes wave activity is often found over
501 regions where orography could contribute to the forcing: for instance above the southern
502 tip of South America and the Eurasian continent. This agrees with previous studies by

Eckermann and Preusse [1999] and Jiang et al. [2002, 2004b] modeling GW activity found in CRISTA and MLS data with the NRL mountain wave forecast model (NRL-MWFM).

GROGRAT:

Figure 6 shows global maps at 28 km altitude of GROGRAT GW squared temperature amplitudes from Exp. 232 for vertical wavelengths from 5 km to 50 km. The ray traces are calculated for background atmospheres for 12 GMT on days 3, 6, 9, ... and 27 of the respective month in 2003 and 2004. This provides a sufficiently large database to obtain a representative average of meteorological situations including different phases of the QBO. Highly variable tropospheric weather conditions average out, but the preferential phase of the strong quasi-sationary planetary waves in the northern winter is a persistent feature.

It should kept in mind, however, that the GROGRAT modeling assumes a homogeneous and isotropic GW source and therefore does not include strong localized GW sources such as orography or deep convection.

The modeled fields reproduce the observations in many respects, such as the asymmetry between northern and southern hemisphere with respect to the polar vortex and the absence/presence of strong planetary waves modulating the GW activity in the polar vortex. The model results also reproduce the shift of GW activity into the summer hemisphere in the tropics and the symmetry with respect to the equator for the equinoxes. In addition, the simulated seasonal cycle of GW squared amplitudes in the southern polar vortex is quite realistic: an absence of wave activity in January; the build-up of the vortex wave activity in April; strong, almost zonally symmetric wave activity in July; and a decaying vortex disturbed by planetary waves in October. In January measurement and model agree in the position of the high latitude maxima of GW squared amplitudes above

526 eastern Europe and central Asia (30° E – 90° E) and at the east coast of North America.
527 The position of the maxima reflects the preferential phase of the planetary waves and
528 hence the position of the vortex edge in the northern hemisphere winter.

529 However, for northern hemisphere winter the magnitude of GW activity in the model
530 is much smaller than in the observations and the model exhibits a much stronger asym-
531 metry between southern and northern hemisphere winter polar vortex values than the
532 measurements, which show essentially equal peak values for the southern hemisphere in
533 July and the northern hemisphere in January. A possible explanation is that weaker winds
534 in the northern hemisphere are compensated by orographic forcing by the more numerous
535 mountain ranges in the northern hemisphere, for instance the south tip of Greenland,
536 the Norwegian mountain ridge the Alps and the Urals, which are all prominent sources
537 of stratospheric GWs [Eckermann and Preusse, 1999; Dörnbrack and Leutbecher, 2001;
538 Jiang et al., 2004b]. Interestingly, even in this five year climatology we do not find en-
539 hanced amplitudes above the Rocky Mountains, which is in agreement with previous
540 studies [Eckermann and Preusse, 1999; Jiang et al., 2004b]. In contrast to the northern
541 hemisphere, orography is responsible only for a small fraction of the waves observed in
542 the SH winter; that is orographically forced waves above the south tip of South America
543 and the Antarctic Peninsula [Eckermann and Preusse, 1999; Jiang et al., 2002; Ern et al.,
544 2006].

545 Furthermore, the high GW squared amplitudes over the Gulf of Mexico and the Asian
546 monsoon regions are not reproduced, indicating that these are features generated primarily
547 by convective sources rather than by the modulation of GWs by the background winds (cf.
548 discussion of the SABER maps; McLandress et al. [2000]; Preusse et al. [2001]; Jiang et al.

[2004a]; Ern et al. [2004]; Preusse and Ern [2005]). The same likely applies for the observed enhanced GW activity in the tropics/subtropics in January, which is not reproduced by the model (there is a southward shift, but no real enhancement in Figure 6a).

5.2. July maps in stratosphere and mesosphere

SABER:

Figure 7 shows GW squared amplitudes in July, same as Figure 5c, but for altitudes from 40 km to 70 km. At 40 km altitude we find the same subtropical maxima as for 28 km altitude in Figure 5c. These local maxima are somewhat less pronounced with respect to the background GW variances at 50 km, but still noticeable. At 60 km and 70 km altitude, however, the subtropical maximum becomes more band-like (i.e. zonally symmetric) and is shifted further to the north. There are two likely explanations for this behavior. First, as altitude increases waves propagate further away from their sources horizontally. Variance enhancements due to localized sources therefore smear out with increasing altitude. Second, as waves propagate upwards, smaller amplitude waves with less pronounced sources or from a GW background can grow more strongly than waves forced with larger amplitudes closer to the saturation limit, so at higher altitudes they gain comparable amplitudes. The influence of the wind fields by critical level filtering, wind modulation and visibility filter [Preusse et al., 2006] therefore becomes more important for the horizontal distribution than the influence of the sources at higher altitudes.

GROGRAT:

At higher altitudes the simulated GROGRAT amplitudes still largely resembles the observations as can be seen from Figure 8. The absolute values at the respective altitudes

and the relative strength of the southern polar vortex and the northern subtropical maximum agree well with the SABER results in Figure 7. Of course, these source-invariant GROGRAT simulations can neither reproduce the convectively forced GWs above Florida and the Asian Monsoon regions nor the loss of these features with altitude. Further, a general underestimate of GW squared amplitudes in the southern subtropics points to the dilemma of either overestimating the high summer latitudes or underestimating the tropical and subtropical values of the winter hemisphere. This problem has already been discussed in section 4.3 and has been ameliorated but not eliminated by the new launch distribution. The GROGRAT results without the vertical wavelength visibility filter applied (not shown) are very similar in their global distributions and only have an offset of less than 1 dB. This indicates that critical level filtering and wind modulation are the dominant processes in shaping the distributions observed by SABER (Figure 7).

5.3. Time series of zonal mean squared amplitudes

Figure 9 compares time series of zonal mean squared GW amplitudes measured by SABER (left column) with the results from GROGRAT Exp. 232 (right column). Again, the GROGRAT results average every third day of the respective months in 2003 and 2004. Results at altitudes between 30 km and 90 km are shown and observed and modeled structures agree in their salient features.

At 30 km altitude, SABER observes high GW squared amplitudes in the winter polar vortices. They contrast with very low GW activity in the summer mid and high latitudes. In the tropics and subtropics, the phase of the annual cycle is reversed and maxima for the SABER measurements are found after the summer solstice, i.e. values are maximum in July and August in the northern hemisphere and maximum in January and February

592 in the southern hemisphere. The high latitude maxima shift to early winter at 50 km
593 altitude whereas the subtropical maximum remains fixed in time. This is in agreement
594 with Fig. 2f of Krebsbach and Preusse [2007], which shows the altitude-latitude variations
595 of the maximum of the annual cycle deduced from SABER GW analyses. Krebsbach and
596 Preusse [2007] find a downward progression of the phase (time) of the high latitude wave-
597 variance maximum in the polar vortices but an almost constant phase of the subtropical
598 maximum throughout the entire stratosphere.

599 The GROGRAT modeling reproduces the enhanced wave amplitudes in the winter po-
600 lar vortices well, and also the shift towards earlier months at increasing altitude. The
601 hemispheric asymmetry between the very large GW squared amplitudes in the southern
602 hemisphere winter polar vortex and the somewhat weaker values in the northern hemi-
603 sphere winter polar vortex is even more pronounced in the GROGRAT model results. As
604 discussed in section 5.1, a potential explanation is that the GROGRAT simulation does
605 not take into account the enhanced forcing of GWs by orography in the north relative to
606 the south.

607 The subtropical maximum is less pronounced in the GROGRAT modeling than in the
608 observations. The difference further supports the assumption that the observed maxima
609 are caused to a large extent by convection during the monsoon and above regions of high
610 sea surface temperature (SST), as has been found from correlations of GWs to cloud
611 proxies and SST [McLandress et al., 2000; Preusse et al., 2001; Jiang et al., 2004a; Ern et
612 al., 2004; Preusse and Ern, 2005].

613 At 70 km altitude (Figure 9e and f) the summertime subtropical maxima extend further
614 poleward and the maxima associated with the polar vortex extend further equatorward.

At 30-40° latitude this yields to a clear semiannual variation of GW variances with paeks at the solstices, in general agreement with radar measurements of gravity wave wind variances in this latitude and height vicinity [Vincent and Fritts, 1987; Thorsen and Franke, 1998; Gavrilov et al., 2000]. The GROGRAT results reproduce semiannual variability at these latitudes, but with a stronger annual component. We will discuss this feature in more detail in section 6.

At 95 km altitude the GROGRAT model results underestimate the SABER values by about 4 dB. The most interesting feature in both measurements and model results is a high latitude summer maximum in the northern hemisphere. In the south, SABER shows a more semiannual variation with similar peaks in summer and winter, whereas GROGRAT produces a summer maximum like for the northern hemisphere and ownly a very weak maximum in winter. The SABER feature is particularly interesting since ground-based radar data at high latitudes [Dowdy et al., 2007] show a semiannual variation at 80 km and winter maxima at 90 km for shorter period waves (<120 minutes; Fig 7 of Dowdy et al. [2007]) and a mixture of semiannual and annual variation at both altitudes, but strongly dependent on location, for longer period waves (120-480 minutes; Fig 8 of Dowdy et al. [2007]). Similar results are also reported by Beldon and Mitchell [2008]. This suggests that the seasonal variation at these altitudes differs for different parts of the GW spectrum and that SABER sees different waves than both spectral windows of the Radar measurements.

Which part of the GW spectrum can cause a phase reversal of the annual cycle observed in high latitude SABER data between 70 km and 95 km altitude? Figure 10 compares time series of slow (SCEs 4 and 8, cf. Table 1) and fast (SCEs 16 and 18) mesoscale waves as well as fast long horizontal wavelength waves (SCEs 22 and 23) for 80 and 95 km

altitude. At 80 km altitude, all SCEs exhibit a wintertime maximum at mid and high latitudes. The wind reversal between 80 km and 95 km altitude removes most of the very slow waves (SCE 4; c =10 ms^{-1}) and reduces the GW squared amplitudes of SCE 8 with c =30 ms^{-1} phase speed. However, the remaining GW activity of these slower waves still has a wintertime maximum also at 95 km altitude. With increasing phase speed (SCEs 16 and 18; c =51 ms^{-1} and c =90 ms^{-1}) a pronounced summertime maximum arises for the mesoscale waves. This is not the case, however, for the long horizontal wavelength waves (SCEs 22 and 23; λ_x =2000 km) though they are comparable in amplitude and phase speed (c =60 ms^{-1}) with the fast mesoscale waves.

Hence, only the fast, medium wavelength GWs can cause the phase reversal and the fact that we observe the phase reversal in the measurements as well as in the composite experiment shows that these waves dominate the upper altitudes in the SABER measurements as well as in the model.

The reproduction of the reversal of the annual cycle around the mesopause by Exp. 232 therefore supports that the intermittency factors have been tuned to broadly realistic values. Also, since we did not use the annual cycle for tuning the intermittency factors, the physical explanation increases confidence that the interpretation of the residual temperature fluctuations in terms of GWs still makes sense around the mesopause and in the lower thermosphere.

6. Propagation direction and distance, momentum flux and mean flow acceleration

As pointed out in section 4, the choice of wave components and intermittency factors is based only on tuning to boreal summer results. In section 5, the annual cycle of GW

squared amplitudes from SABER therefore provides an independent observation to test the adequacy of the resulting simulations. The good agreement found between observations and model results supports the choice of SCEs and intermittency factors deduced from boreal summer observations. Though there are still deviations between the observations and the model results, probably mainly due to missing GW sources, we have now gained sufficient confidence in the model results that we can infer quantities which cannot be measured directly.

6.1. Time series of zonal propagation direction

An open question is the nature of the strong mid-latitude semiannual variation in GW squared amplitudes found in the mesosphere. Krebsbach and Preusse [2007] spectrally analyzed a four-year data series of root mean square (RMS) zonal averages. Around 70 km they found about 2.0-2.5 K semiannual amplitude for 40° latitude in both hemispheres, but only 0.5-1.0 K semiannual amplitude in the tropics where we expect to find modulation of GWs by the well-known mesospheric semiannual oscillation (SAO) in the tropical zonal winds [Hirota, 1978; Burrage et al., 1996]. Krebsbach and Preusse [2007] speculated that the variations at 40° latitude are not SAO signals but rather an annual cycle, if GW momentum fluxes are considered.

The general argument can be understood by reconsidering the altitude evolution of the annual cycle shown in Figure 9. At 30 km and 50 km altitude (Figure 9a, c) there is a subtropical summer maximum southward of 30° N and a mid and high latitude winter maximum northward 30° N. For the summer maximum we expect preferential eastward propagation opposite to easterly background winds and for the winter maximum we expect preferential westward propagation opposite to westerly background winds. At 70 km

altitude (Figure 9e) the GW activity related to the polar vortex spreads equatorward and the subtropical maximum spreads poleward to overlap between 25° N and 50° N. The two maxima result in a semiannual component, however since we expect opposite preferential propagation directions the momentum flux points in opposite directions and for momentum flux we would observe an annual cycle. We test this hypothesis by calculating the average zonal momentum flux from the GROGRAT simulations, which is shown in Figure 11.

The color scale in Figure 11 indicates the absolute value of the zonal momentum flux, overplotted solid lines indicate positive values, i.e. preferentially eastward propagating waves, overplotted dashed lines indicate negative values, i.e. preferentially westward propagating waves. As expected, waves propagate preferentially eastward against the subtropical easterly jet in the summer of the respective hemisphere and preferentially westward against the polar vortex jet in winter. At the equinoxes, the average zonal momentum flux vanishes. Figures 9e and f still show significant GW activity at these times, i.e. the vanishing zonal momentum flux is caused by flux cancellation caused by GWs propagating in different directions rather than by an absence of waves. This interpretation is supported by ground-based radar measurements over Japan (35°N, 136°E). Tsuda et al. [1990] find a strong summer and a weaker winter peak in GW wind fluctuations with still considerable amplitudes at equinoxes. The winter peak is associated with negative, i.e. westward momentum flux, the summer peak with positive, i.e. eastward momentum flux. The relative stronger summer maximum is compatible with the position of the MU radar close to the localized GW forcing due to the Asian monsoon.

6.2. Mean-flow acceleration

703 The GW-induced mean-flow forcing is given by Eq. 42 of Fritts and Alexander [2003]:

$$\left(\bar{X}, \bar{Y}\right) = -\frac{\epsilon}{\bar{\rho}} \frac{\partial}{\partial z} \left(F_{px}, F_{py}\right), \tag{5}$$

704 where (F_{px}, F_{py}) is the horizontal vector of the vertical flux of GW momentum, $\bar{\rho}$ is the
705 density of the background atmosphere, and $\left(\bar{X}, \bar{Y}\right)$ an acceleration term for the back-
706 ground flow. Conventionally, the equation contains an intermittency factor ϵ reflecting
707 the fact that GWs might not always be present in the atmosphere. We calculate the
708 acceleration for the GROGRAT composites as follows

$$\left(\bar{X}, \bar{Y}\right) = -\frac{1}{\bar{\rho}} \frac{1}{J} \sum_i \epsilon_i \frac{\partial}{\partial z} \left(F_{px,i}, F_{py,i}\right) \tag{6}$$

709 where J is the number of the individual GWs i in the considered bin (e.g. latitude bin at
710 fixed altitude for zonal means) and ϵ_i is an intermittency factor associated with this wave
711 according to Table 1. Note that in this way the final obliteration of a wave near a critical
712 level does in our calculations not contribute to the acceleration, because we do not take
713 into account the disappearance of waves between different altitude levels. However, the
714 error due to this neglect is small, since the wave looses its momentum almost completely
715 below: the vertical wavelength, and therefore the saturation amplitude, becomes very
716 small before the GW encounters the critical level.

717 In GROGRAT the waves can be horizontally refracted by horizontal gradients of the
718 background atmosphere [Marks and Eckermann, 1995]. Therefore there are two different
719 mechanisms for transferring momentum to the mean flow. First, the waves can dissipate

by wave breaking or turbulent and radiative dissipation. In this case, the acceleration is given by the vertical gradient of the absolute value of momentum flux $|F_p|$ in the direction of the horizontal wave vector (k, l)

$$\begin{aligned}\left(\bar{X},\bar{Y}\right)_{diss} &= -\frac{1}{\bar{\rho}}\frac{1}{J}\sum_i \epsilon_i \frac{(k_i,l_i)}{k_i^2+l_i^2}\frac{\partial}{\partial z}|F_{p,i}| \\ &= -\frac{1}{\bar{\rho}}\frac{1}{J}\sum_i \epsilon_i \left(\cos(\phi_i),\sin(\phi_i)\right)\frac{\partial}{\partial z}|F_{p,i}|, \end{aligned} \quad (7)$$

where ϕ is the direction of the wave vector defined counterclockwise from due east (ϕ =0). Second, waves can change their horizontal propagation direction. For instance, a wave propagating northeastward might be aligned more zonally with increasing altitude due to lateral refraction. In this case, the wave carries less meridional and more zonal momentum. The acceleration is then expressed by the change of the wave direction and the acceleration by horizontal wave refraction is

$$\left(\bar{X},\bar{Y}\right)_{turn} = -\frac{1}{\bar{\rho}}\frac{1}{J}\sum_i \epsilon_i |F_{p,i}| \frac{\partial}{\partial z}\left(\cos(\phi_i),\sin(\phi_i)\right) \quad (8)$$

In addition to these two mechanisms there are further effects in GW theory which influence the momentum and amplitudes of GWs. When GWs are refracted by horizontal gradients also the absolute value of the horizontal wavelength and the area covered by the wave-packet change. These two effects would have to be considered simultaneously, but the geometric spreading effect cannot be incorporated easily into a model based on a very limited number of single rays. We therefore decided to neglect these effects and first investigate the GW forcing mechanisms described above.

Figure 12 shows zonal mean accelerations for composite 232 for 15 July 2003. It should be noted that we do not apply SABER visibility filters for these acceleration fields. The left column shows the acceleration in the zonal direction and the right column the acceleration in the meridional direction. All waves which do not propagate purely zonally or purely meridionally contribute to both forcing terms. The uppermost row shows the total acceleration from Equ. (6). Values of $\bar{X}$ (Figure 12a) can reach up to 250 $ms^{-1}day^{-1}$ at the summer mesopause (we clipped the color scale in order to better visualize the accelerations in the upper stratosphere and lower mesosphere). This is of the same order but at the high end of the acceleration values generally reported from GCM and GW parameterization studies (e.g. McLandress [1998]; Charron et al. [2002]; McLandress and Scinocca [2005]).

The GROGRAT simulations include only medium- and large-scale GWs visible to SABER and do not include the short horizontal wavelength waves observed by airglow imagers (e.g. Fritts and Alexander [2003]; Preusse et al. [2008]). Does the fact that the observed waves are already sufficient to explain all the wave forcing needed by the GCMs imply that medium and large horizontal wavelength GWs exclusively drive the MLT? When considering these values we should keep in mind that the GW accelerations shown are a pure forward result from the tuning of the launch values and intermittency factors by the measured GW-amplitudes from SABER in July and some further constraints on GW momentum flux measurements in the stratosphere.

As pointed out above, there is in particular a complete lack of constraints on the horizontal wavelength distribution in the mesosphere and thus there still remains great freedom for tuning. In addition, in our study some serious assumptions are made. For instance,

759 we do not consider any processes that could transport momentum away from the dissi-
760 pation regions such as secondary wave generation [Vadas and Fritts, 2002] or non-linear
761 wave interaction, for example, by triads [Bittner et al., 1997; Wüst and Bittner, 2006].
762 We also assume that all waves propagate upward whereas in the real atmosphere at least
763 some waves will propagate downward. The fraction of downward propagating waves is
764 less than 20 % according to data from radio sondes and radars for the lower stratosphere
765 (e.g. Wang et al. [2005]; Vaughan and Worthington [2007]) and falling sphere data for
766 the mid and upper stratosphere (e.g. Eckermann and Vincent [1989]). It should be noted
767 in this context that wave reflection occurs when the intrinsic frequency $\hat{\omega}$ approaches the
768 buoyancy frequency and does not occur to any great extent for the mesoscale and long
769 horizontal wavelength (>100 km) GWs observed by IR limb sounders considered in this
770 study (cf. Kim et al. [2003]; Fritts and Alexander [2003]; Preusse et al. [2008]). Down-
771 ward propagating waves in this wavelength regime therefore can only originate from high
772 altitude sources.

773 For the above-mentioned reasons, our acceleration values are likely overestimated. Short
774 horizontal wavelength GWs observed by airglow imagers are also known to carry significant
775 momentum [Tang et al., 2005]. Short and medium horizontal wavelength GWs therefore
776 both contribute to driving the wind systems and circulation in the MLT. The uncertain-
777 ties of this study are too large to definitively address the relative role of the different
778 wavelength regimes quantitatively. However, the results shown suggest that medium- and
779 large-scale gravity waves are important.

780 Figure 12b shows the meridional acceleration $\bar{Y}$. The meridional accelerations are about
781 a factor three smaller (again the color scale is clipped in order to highlight structures in

the upper stratosphere and mesosphere). The fact that the meridional accelerations are smaller than the zonal accelerations is caused by the preferentially zonal direction of the mean flow.

The middle row shows the contribution due to refraction by horizontal wind gradients calculated from Eq. (8). The lowermost row gives the relative contribution of this term to the total forcing. Relative values are only shown if the total acceleration is larger than 5 $ms^{-1}day^{-1}$. The zonal acceleration by horizontal refraction (Figure 12c) remains smaller than 5 $ms^{-1}day^{-1}$ and contributes less than 5 % of the total zonal mean flow acceleration (Figure 12e). Thus from the zonal GW induced forcing alone this effect could be neglected. Similar conclusions were drawn by Hasha et al. [2008]. However, the absolute values as well as the relative contributions in the meridional direction are larger (Figure 12d, f). Relative contributions of horizontal refraction to the meridional forcing can exceed 50 %. By comparing panels b) and d) it can be seen that horizontal refraction acts at different locations and sometimes counteracts acceleration by dissipation.

6.3. Zonal propagation

Gravity wave parameterization schemes operated in GCMs generally assume that GWs propagate upward in the vertical column of a GCM grid point. (There is one exception: the ray-tracing parameterization of convectively generated GWs by Song and Chun [2008].) However, since the GWs we consider have much longer horizontal than vertical wavelengths we can expect that they cover considerable distances in the horizontal when propagating from the troposphere into the mesosphere. An indication of this is given in Figure 1. Some of the waves shown traverse 40° or more in latitude. However, is this rep-

resentative and are the waves that propagate over large distances the same waves which carry large momentum flux?

Zonal means of the difference in latitude between the launch location and the actual position of the GW rays in the atmosphere are shown in Figure 13. Negative values indicate that the waves preferentially originate from sources northward of the observation latitude (i.e. southward-propagating waves), positive values indicate that the rays originate preferentially from the south (i.e. northward propagation). Low values can indicate a zonal alignment of the wave vectors and fast upward propagation or a balance between northward- and southward-propagating waves.

At very high latitudes we are close to the model grid boundaries and GWs propagating toward the lateral boundaries, i.e. poleward-propagating GWs, cannot be compensated by waves propagating in the opposite direction, since these waves would need to originate from outside the grid. The high values observed at very high latitudes (>60°) are therefore artificial and in the following we discuss low and mid latitudes (<60°) only.

As expected, the average latitude shift increases with increasing altitude in Figure 13. A large part is contributed by long horizontal wavelength waves which can exist at low altitudes only in the tropics and spread poleward with increasing altitude (cf. Figure 2i). Consequently, when weighting the latitudinal shift by the momentum flux of the waves (Figure 13b), the values are strongly reduced. However, when weighting the latitudinal shift by the accelerations, in particular in the stratosphere and lower mesosphere the slower waves are emphasized and the latitudinal shift is enhanced. Even though accelerations at these altitudes are small they could contribute significantly to the branch of the Brewer-Dobson circulation in the summer hemisphere [Alexander and Rosenlof, 2003].

7. Summary and Discussions

In this paper, we derived a climatology of GW squared amplitudes from the Sounding of the Atmosphere using Broadband Emission Radiometry (SABER) temperatures mapping a five-year time series to calendar months. Many salient features are compatible with previous observations from different satellites showing these features to be persistent from year to year.

The GW measurements are compared to results of global ray tracing simulations employing the Gravity wave Regional Or Global RAy Tracer (GROGRAT). Based on SABER zonal mean GW squared amplitudes for July and CRISTA momentum flux values, a homogeneous and isotropic launch distribution is iteratively tuned to best reproduce these observations.. The resulting launch distribution contains different phase speed medium horizontal wavelength GWs, some of very high phase speed and extremely low amplitudes, as well as long horizontal wavelength GWs of several thousand kilometer wavelength. Waves are launched in eight equispaced azimuth directions at 5 km altitude.

The tuning of the launch distribution is based on zonal means of SABER GW squared amplitudes for July and CRISTA absolute values of momentum flux, only. Thereafter, no additional tuning is performed, and thus longitudinal structures seen in both measured and modeled global maps as well as time series of the annual cycle provide independent tests. The good agreement found in e.g. reproducing observed seasonal variations raises confidence in the tuned GW launch parameters. In particular, the modeled time series reproduce an observed reversal of the phase of the annual cycle between 80 km and 95 km altitude. This phase reversal is attributed to medium-scale horizontal wavelength GWs with ground-based horizontal phase speeds greater than 50 ms^{-1}.

Based on this cross-validated observation-tuned model run, we can calculate quantities which cannot be directly measured by SABER and are speculated to be major sources of uncertainty in current GW parameterization schemes. Two examples shown in this paper are the average cross-latitude propagation of GWs and the relative acceleration contributions provided by saturation and dissipation, on the one hand, and the horizontal refraction of GWs by horizontal gradients of the mean flow, on the other hand.

The average cross-latitude propagation reaches peak values of about 15°. Long horizontal wavelength waves carrying little momentum largely contribute to this value and as a consequence momentum-flux-weighted mean values are much lower. However, acceleration-weighted values show up to 25° average cross-latitude propagation in the stratosphere and lower mesosphere. Though these accelerations are small in absolute value they can provide an important contribution to the summer-hemisphere branch of the Brewer-Dobson circulation [Alexander and Rosenlof, 2003]. In a changing climate, the wind fields in the troposphere and stratosphere will change. A propagation path of the waves that differs from the one assumed in tuning the parameterization scheme for the needs of the GCM then might induce an incorrect response to climate change.

Both zonal and meridional GW induced mean-flow acceleration values in the GROGRAT simulations are of the same order but at the upper end of the range known from GCM and GW parameterization scheme studies. Error ranges are high, however, since we have very few constraints on the horizontal wavelength distributions in particular of the fast waves carrying large momentum fluxes into the MLT. In addition, the current approach neglects processes which could carry away momentum flux from regions of wave instability, such as secondary wave generation.

871 Despite these caveats we have a sufficiently realistic simulation to test whether the hori-
872 zontal refraction of GWs by horizontal gradients of the background winds is an important
873 effect on a global scale compared to momentum deposition by wave dissipation. Mean
874 flow forcing by horizontal refraction was introduced by Bühler and McIntyre [2003] as a
875 new mechanism acting at different locations and in a different way than wave dissipation
876 via a process they referred to as "remote recoil". However, Bühler and McIntyre [2003]
877 provided only a theoretical explanation of the effect and did not estimate the relative
878 magnitude compared to wave dissipation in the real atmosphere. We here find that the
879 effect is smaller than 5 % for zonal acceleration in agreement to small influeces reported
880 by Hasha et al. [2008]. However, the effect is up to 50 % in meridional acceleration and
881 therefore merits further consideration.

882 The GROGRAT model results match the observed distributions well. However, they
883 give no hint on the physical nature of the assumed homeogeneous and isotropic sources.
884 In addition, global maps already indicate missing localized sources such as orography and
885 deep convection. In future, we therefore will need to replace a tuned parameterized source
886 distribution by real understanding of lower-atmospheric source distributions..

887 In order to reach this aim a better characterization of the observed waves is required
888 [Alexander and Barnet, 2007; Eckermann et al., 2007]. Major sources of uncertainty for
889 the current study are horizontal wavelength distributions and characteristics of propaga-
890 tion direction. Some first attempts to investigate horizontal wave structures were made
891 by Eckermann and Preusse [1999] and Preusse et al. [2002], and recently some interesting
892 studies have been based on nadir viewing instruments [Wu and Zhang, 2004; Alexander
893 and Barnet, 2007; Eckermann et al., 2006, 2007]. However, nadir viewing satellites can

capture only a small part of the vertical wavelength distribution and only at the low altitudes (less than 40 km) where they are sensitive. What is urgently needed is an instrument with the good vertical resolution of a limb sounder and the good horizontal mapping of a nadir viewing instrument. Employing infrared limb-imaging such an instrument can be built based on recent advances in detector technology [Riese et al., 2005; Friedl-Vallon et al., 2006].

8. Acknowledgments

Jens Oberheide is supported under DFG CAWSES Grant OB 299/2-2. Part of the work of Manfred Ern was supported by DFG CAWSES Grant ER 474/1-1. Richard H. Picard acknowledges support from the NASA SABER Program Office and from Dr. Kent Miller of the U.S. Air Force Office of Scientific Research.

References

Achatz U. (2007), The primary nonlinear dynamics of modal and nonmodal perturbations of monochromatic inertia-gravity waves, J. Atmos. Sci., 64, 74-95.

Alexander, M. J. (1998), Interpretations of observed climatological patterns in stratospheric gravity wave variance. J. Geophys. Res. 103, 8627-8640.

Alexander, M. J., and T. J. Dunkerton (1999), A spectral parameterization of mean-flow forcing due to breaking gravity waves, *J. Atmos. Sci., 56*, 4167-4182.

Alexander, M. J., Tsuda, T., Vincent R.A. (2002), On the latitudinal variations observed in gravity waves with short vertical wavelengths. J. Atmos. Sci. 59, 1394-1404.

Alexander, M. J., and K. H. Rosenlof (2003), Gravity-wave forcing in the stratosphere: Observational constraints from the Upper Atmosphere Research Satellite and implications for parameterization in global models, *J. Geophys. Res., 108*, 4597, doi:10.1029/2003JD003373.

Alexander, M. J., and C. Barnet (2007), Using satellite observations to constrain parameterizations of gravity wave effects for global models, J. Atmos. Sci., 64, 1652-1665.

Alexander, M. J., J. Gille, C. Cavanaugh, M. Coffey, C. Craig, V. Dean, T. Eden, G. Francis, C. Halvorson, J. Hannigan, R. Khosravi, D. Kinneson, H. Lee, S. Massie, B. Nardi, A. Lambert, (2008), Global estimates of gravity wave momentum flux from high resolution dynamics limb sounder (HIRDLS) observations, *J. Geophys. Res., 113*, D15S18, doi:10.1029/2007JD008807.

Allen, S. J., and R. A. Vincent (1995), Gravity wave activity in the lower atmosphere: Seasonal and latitudinal variations, *J. Geophys. Res., 100*, 1327-1350.

925 Beldon, C.L. and N.J. Mitchell (2008), Gravity waves in the polar mesopause region
926 observed by meteor radar, *J. Atmos. Sol.-Terr. Phys.*, submitted.

927 Bittner, M., D. Offermann, and H. U. Widdel (1997), Nonlinear resonant interaction of
928 atmospheric gravity waves derived from chaff-wind data: a case study, Proceedings 13th
929 ESA Symposium on European Rocket and Balloon Programmes and Related Research,
930 Öland, Sweden, 26-29 May 1997, ESA SP-397, pp 489-494.

931 Borsche, M., G. Kirchengast, and U. Foelsche (2007), Tropical tropopause climatology
932 as observed with radio occultation measurements from CHAMP compared to ECMWF
933 and NCEP analyses, *Geophys. Res. Lett., 34*, L03702, doi:10.1029/2006GL027918.

934 Bühler, O. and M. E.McIntyre (2003), Remote recoil: a new wave-mean interaction effect,
935 *J. Fluid Mech., 492*, 207-230.

936 Burrage, M. D., R. A. Vincent, H. G. Mayr, W. R. Skinner, N. F. Arnold and P. B.
937 Hays (1996), Long-term variability in the equatorial middle atmosphere zonal wind, *J.*
938 *Geophys. Res., 101*, 12,847-12,854.

939 Charron M., E. Manzini, and C. D. Warner (2002), Intercomparison of gravity wave pa-
940 rameterizations: Hines Doppler-spread and Warner and McIntyre ultra-simple schemes,
941 *J. Met. Soc. Japan, 80*, 335-345.

942 Chimonas, G. (1999), Reply to comments on "Waves and the middle atmosphere wind
943 irregularities", *J. Atmos. Sci., 39*, 2,041-2,042.

944 de la Torre, A., T. Schmidt and J. Wickert (2006), A global analysis of wave potential
945 energy in the lower and middle atmosphere from CHAMP and SAC-C GPS-RO long
946 term data, Geophys. Res. Lett., 33, L24809, doi:10.1029/2006GL027696.

947 Dewan, E. M. and R. E. Good (1986), Saturation and the "universal" spectrum for vertical
948 profiles of horizontal scalar winds in the atmosphere, *J. Geophys. Res., 91*, 2,742-2,748.
949 Dörnbrack, A. and M. Leutbecher (2001), Relevance of mountain wave cooling for the
950 formation of polar stratospheric clouds over Scandinavia: A 20 year climatology, *J.*
951 *Geophys. Res., 106*, 1583-1593.
952 Dowdy, A. J., R. A. Vincent, M. Tsutsumi, K. Igarashi, Y. Murayama, W. Singer,
953 and D. J. Murphy (2007), Polar mesosphere and lower thermosphere dynamics:
954 1. Mean wind and gravity wave climatologies, *J. Geophys. Res., 112*, D17104,
955 doi:10.1029/2006JD008126.
956 Dunkerton, T.J. (1997), The role of gravity waves in the quasi-biennial oscillation, *J.*
957 *Geophys. Res., 102*, 26,053-26,076.
958 Eckermann, S.D. and R.A. Vincent (1989), Falling sphere observations of anisotropic
959 gravity wave motions in the upper stratosphere over Australia *Pure Appl. Geophys.,*
960 *130*, 509-532.
961 Eckermann, S. D. (1992), Ray-tracing simulation of the global propagation of inertia
962 gravity waves through the zonally averaged middle atmosphere, *J. Geophys. Res., 97*,
963 15,849-15,866, 1992.
964 Eckermann, S. D., I. Hirota, and W K. Hocking (1995), Gravity wave and equatorial
965 wave morphology of the stratosphere derived from long-term rocket soundings, *Quart.*
966 *J. Roy. Met. Soc., 121*, 146-186.
967 Eckermann, S. D. and C. J. Marks (1997), GROGRAT: a new model of the global prop-
968 agation and dissipation of atmospheric gravity waves, *Adv. Space Res., 20*, 1253-1256.

969 Eckermann, S.D. and P. Preusse (1999), Global measurements of stratospheric mountain
970 waves from space, *Science, 286*, 1534-1537.

971 Eckermann, S. D., D. L. Wu, J. D. Doyle, J. F. Burris, T. J. McGee, C. A. Hostetler, L.
972 Coy, B. N. Lawrence, A. Stephens, J. P. McCormack, and T. F. Hogan (2006), Imaging
973 gravity waves in lower stratospheric AMSU-A radiances, Part 2: validation case study,
974 *Atmos. Chem. Phys., 6*, 3343-3362.

975 Eckermann, S. D., J. Ma, D. L. Wu, and D. Broutman (2007), A three-dimensional
976 mountain wave imaged in satellite radiance throughout the stratosphere: Evidence of
977 the effects of directional wind shear, *Quart. J. Roy. Meteorol. Soc., 133*, 1959-1975.

978 Ern, M., P. Preusse, M.J. Alexander, and C.D. Warner (2004), Absolute values of grav-
979 ity wave momentum flux derived from satellite data. *J. Geophys. Res., 109*, D20103,
980 doi:10.1029/2004JD004752.

981 Ern, M., P. Preusse, and C.D. Warner (2006), Some experimental constraints for spectral
982 parameters used in the Warner and McIntyre gravity wave parameterization scheme,
983 *Atmos. Chem. Phys., 6*, 4361-4381, 2006.

984 Ern, M., P. Preusse, M. Krebsbach, M. G. Mlynczak, and J. M. Russell III (2008), Equa-
985 torial wave analysis from SABER and ECMWF temperatures, *Atmos. Chem. Phys., 8,*
986 845-869.

987 Fetzer, E. J., and J. C. Gille (1994), Gravity wave variances in LIMS temperatures, I,
988 Variability and comparison with background winds, *J. Atmos. Sci., 51,* 2461-2483.

989 Friedl-Vallon, F., M. Riese, G. Maucher, A. Lengel, F. Hase, P. Preusse, and R. Spang
990 (2006), Instrument concept and preliminary performance analysis of GLORIA, *Adv.*
991 *Space Res., 37*, 2287-2291.

992 Fritts, D. C. (1984), Gravity Wave Saturation in the Middle Atmosphere: A Review of
993 Theory and Observations, *Rev. Geophys., 22*, 275-308.

994 Fritts, D. C. and Alexander, M. J. (2003), Gravity wave dynamics and effects in the
995 middle atmosphere. *Rev. Geophys. 41*, art. no. 1003.

996 Gavrilov, N.M., S. Fukao, and T. Nakamura (2000), Gravity wave intensity and momen-
997 tum fluxes in the mesosphere over Shigaraki, Japan (35N, 136E) during 1986-1997, *Ann.*
998 *Geophys., 18*, 834-843.

999 Grossmann, K. U., D. Offermann, O. Gusev, J. Oberheide, M. Riese, and R. Spang (2002),
1000 The CRISTA-2 Mission, *J. Geophys. Res., 107*, 8173, doi:10.1029/2001JD000667.

1001 Hagan, M. E., J. M. Forbes, and F. Vial (1995), On Modeling Migrating Solar Tides,
1002 *Geophys. Res. Lett. 22*, 893-896.

1003 Hasha, A., O. Bühler, and J. Scinocca (2008), Gravity wave refraction by three-
1004 dimensionally varying winds and the global transport of angular momentum, *J. Atmos.*
1005 *Sci.*, in press.

1006 Hertzog, A., G. Boccara, R. A. Vincent, F. Vial, and Ph. Coquerez (2008), Estimation of
1007 gravity-wave momentum flux and phase speeds from long-duration stratospheric balloon
1008 flights. 2: Results from the Vorcore campaign in Antarctica, *J. Atmos. Sci.,* in print.

1009 Hines, C. O. (1997), Doppler-spread parameterization of gravity-wave momentum deposi-
1010 tion in the middle atmosphere. Part1: Basic formulation, *J. Atmos. Solar-Terr. Phys.,*
1011 *59*, 371-386.

1012 Hines, C. O. (1999), Comments on "Waves and the middle atmosphere wind irregulari-
1013 ties", *J. Atmos. Sci., 39*, 2,038-2,040.

Hirota, I. (1978), Equatorial waves in upper stratosphere and mesosphere in relation to semiannual oscillation of zonal wind, *J. Atmos. Sci., 35*, 714-722.

Holton, J.R. (1982), The Role of Gravity Wave Induced Drag and Diffusion in the Momentum Budget of the Mesosphere, *J. Atmos. Sci., 39*, 791-799.

Jiang, J. H., D. L. Wu, and S. D. Eckermann (2002), Upper Atmosphere Research Satellite (UARS) MLS observations of mountain waves over the Andes, *J. Geophys. Res., 107*, 8273, doi:10.1029/2002JD002091.

Jiang, J. H., B. Wang, K. Goya, K. Hocke, S. D. Eckermann, J. Ma, D. L. Wu, and W. J. Read (2004a), Geographical distribution and interseasonal variability of tropical deep convection: UARS MLS observations and analyses, *J. Geophys. Res., 109*, D03111, 10.1029/2003JD003756.

Jiang, J. H., S. D. Eckermann, D. L. Wu, and J. Ma (2004b), A search for mountain waves in MLS stratospheric limb radiances from the winter Northern Hemisphere: Data analysis and global mountain wave modeling, *J. Geophys. Res. 109*, D03107, doi:10.1029/2003JD003974.

Kim Y. J., S. D. Eckermann, and H.-Y. Chun (2003), An overview of the past, present and future of gravity-wave drag parametrization for numerical climate and weather prediction models - Survey article, *Atmosphere-Ocean, 41*, 65-98.

Krebsbach, M. and P. Preusse (2007), Comparison of global distributions of zonal-mean gravity wave variance inferred from different satellite measurements, *Geophys. Res. Lett., 34*, L03814, doi:10.1029/2006GL028040.

Kutepov, A. A., A. G. Feofilov, B. T. Marshall, L. L. Gordley, W. D. Pesnell, R. A. Goldberg, and J. M. Russell III (2006), SABER temperature observations in the summer

polar mesosphere and lower thermosphere: Importance of accounting for the CO2 $\nu 2$ quanta V-V exchange, *Geophys. Res. Lett., 33*, L21809, doi:10.1029/2006GL026591.

Manzini, E., and N. A. McFarlane (1998), The effect of varying the source spectrum of a gravity wave parameterization in a middle atmosphere general circulation model, *J. Geophys. Res., 103*, 31,523-31,539.

Marks, C. J., and S. D. Eckermann (1995), A Three-Dimensional Nonhydrostatic Ray-Tracing Model for Gravity Waves: Formulation and Preliminary Results for the Middle Atmosphere, *J. Atmos. Sci., 52*, 1959-1984.

McLandress, C. (1998), On the importance of gravity waves in the middle atmosphere and their parameterization in general circulation models, *J. Atmos. Sol.-Terr. Phys., 60*, 1357-1383.

McLandress, C., M. J. Alexander and D. L. Wu (2000), Microwave Limb Sounder observations of gravity waves in the stratosphere: a climatology and interpretation, *J. Geophys. Res., 105*, 11,947-11,967.

McLandress C. and J. F. Scinocca (2005), The GCM response to current parameterizations of nonorographic gravity wave drag, *J. Atmos. Sci., 62*, 2394-2413.

Medvedev A. S. and G. P. Klaassen (2000), Parameterization of gravity wave momentum deposition based on nonlinear wave interactions: basic formulation and sensitivity tests, *J. Atmos. Sol.-Terr. Phys., 62*, 1015-1033.

Mertens, C. J., M. G. Mlynczak, M. Lopez-Puertas, P. P. Wintersteiner, R. H. Picard, J. R. Winick, L. L. Gordley, and J. M. Russell III (2001), Retrieval of mesospheric and lower thermospheric kinetic temperature from measurements of CO_2 15 μm Earth limb emission under non-LTE conditions, *Geophys. Res. Lett., 28*, 1391-1394.

Mertens, C. J., F. J. Schmidlin, R. A. Goldberg, E. E. Remsberg, W. D. Pesnell, J. M. Russel III, M. G. Mlynczak, M. Lopez-Puertas, P. P. Wintersteiner, R. H. Picard, J. R. Winick, and L. L. Gordley (2004), SABER observations of mesospheric temperatures and comparisons with falling sphere measurements taken during the 2002 summer MaCWAVE campaign, *Geophys. Res. Lett., 31*, L03105, doi:10.1029/2003GL018605.

Mlynczak, M.G. (1997), Energetics of the mesosphere and lower thermosphere and the SABER experiment, *Adv. Space Res. 20 (6)*, 1177-1183.

Oberheide, J., Q. Wu, T. L. Killeen, M. E. Hagan, and R. G. Roble (2006), Diurnal nonmigrating tides from TIDI wind data: Monthly climatologies and seasonal variations, *J. Geophys. Res., 111*, A10S03, doi:10.1029/2005JA011491.

Offermann, D., K. U. Grossmann, P. Barthol, P. Knieling, M. Riese, and R. Trant (1999), The CRyogenic Infrared Spectrometers and Telescopes for the Atmosphere (CRISTA) experiment and middle atmosphere variabilitiy, *J. Geophys. Res., 104*, 16,311-16,325.

Preusse, P., G. Eidmann, S. D. Eckermann, B. Schaeler, R. Spang and D. Offermann (2001), Indications of convectively generated gravity waves in CRISTA temperatures, *Adv. Space Res., 27*, 1653-1658.

Preusse, P., A. Dörnbrack, S. D. Eckermann, M. Riese, B. Schaeler, J. Bacmeister, D. Broutman, and K. U. Grossmann (2002), Space based measurements of stratospheric mountain waves by CRISTA, 1. Sensitivity, analysis method and a case study, *J. Geophys. Res., 107*(D23), 8178, doi:10.1029/2001JD000699.

Preusse, P. and M. Ern (2005), Indication of convectively generated gravity waves observed by CLAES, *Adv. Space Res., 35*, doi:10.1016/j.asr.2004.09.005, 1987-1991.

1082 Preusse P., M. Ern, S. D. Eckermann, C. D. Warner, R. H. Picard, P. Knieling, M.
1083 Krebsbach, J. M. Russel III, M. G. Mlynczak, C. J. Mertens, and M. Riese (2006),
1084 Tropopause to mesopause gravity waves in August: measurement and modeling, *J.*
1085 *Atmos. Solar-Terr. Phys., 68*, 1730-1751.

1086 Preusse P., S. D. Eckermann, and M. Ern (2008), Transparency of the atmosphere to
1087 short horizontal wavelength gravity waves, *J. Geophys. Res.*, in press.

1088 Remsberg, E. E., B. T. Marshall, M. Garcia-Comas, D. Krueger, G. S. Lingenfelser, J.
1089 Martin-Torres, M. G. Mlynczak, J. M. Russell III, A. K. Smith, Y. Zhao, C. Brown,
1090 L. L. Gordley, M. J. Lopez-Gonzalez, M. Lopez-Puertas, C.-Y. She, M. J. Taylor and
1091 R. E. Thompson (2008), Assessment of the quality of the Version 1.07 temperature-
1092 versus-pressure profiles of the middle atmosphere from TIMED/SABER, *J. Geophys.*
1093 *Res., 113*, D17101, doi:10.1029/2008JD010013.

1094 Riese, M., R. Spang, P. Preusse, M. Ern, M. Jarisch, D. Offermann, and K. U. Grossmann
1095 (1999), Cryogenic Infrared Spectrometers and Telescopes for the Atmosphere (CRISTA)
1096 data processing and atmospheric temperature and trace gas retrieval, *J. Geophys. Res.,*
1097 *104*, 16,349-16,367.

1098 Riese, M., F. Friedl-Vallon, R. Spang, P. Preusse, C. Schiller, L. Hoffmann, P. Konopka,
1099 H. Oelhaf, T. von Clarmann, M. Höpfner (2005), GLObal limb Radiance Imager for the
1100 Atmosphere (GLORIA): scientific objectives, *Adv. Space Res.,*, 989-995.

1101 Roble, R. G., and E. C. Ridley (1994), A thermosphere-ionosphere-mesosphere-
1102 electrodynamics general circulation model (time-GCM): Equinox solar cycle minimum
1103 simulations (30-500 km), Geophys. Res. Lett., 21, 417-420.

Russell, J. M., III, M. G. Mlynczak, L. L. Gordley, J. Tansock, and R. Esplin (1999), An overview of the SABER experiment and preliminary calibration results, *Proc. SPIE, 3756*, 277-288.

Smith, S. A., D. C. Fritts and T. E. VanZandt (1987), Evidence for a saturated spectrum of atmospheric gravity waves, *J. Atmos. Sci., 44*, 1404-1410.

Song I.-S. and H.-Y. Chun (2008), A lagrangian spectral parameterization of gravity wave drag induced by cumulus convection, *J. Atmos. Sci., 65*, 1204-1224.

Tang J., G. R. Swenson, A. Z. Liu, and F. Kamalabadi (2005), Observational investigations of gravity wave momentum flux with spectroscopic imaging, *J. Geophys. Res., 110*, D09S09, doi:10.1029/2004JD004778.

Thorsen, D., and S. J. Franke (1998), Climatology of mesospheric gravity wave activity over Urbana, Illinois (40N, 88W), *J. Geophys. Res., 103*, 3767-3780.

Tsuda, T., Y. Murayama, M. Yamamoto, S. Kato, and S. Fukao (1990), Seasonal variation of momentum flux in the mesosphere observed with the mu radar, *Geophys. Res. Lett., 17*, 725-728.

Tsuda, T. and K. Hocke (2002), Vertical wave number spectrum of temperature fluctuations in the stratosphere using GPS occultation data, *J Met. Soc. Japan, 80*, 925-938.

Vadas, S. L. and D. C. Fritts (2002), The importance of spatial variability in the generation of secondary gravity waves from local body forces, *Geophys. Res. Lett., 29*, 10.1029/2002GL015574

Vaughan G. and R.M. Worthington (2007), Inertia-gravity waves observed by the UK MST radar, *Q. J. Roy. Met. Soc., 133*, 179-188.

Robert A. Vincent and David C. Fritts (1987), A Climatology of Gravity Wave Motions in the Mesopause Region at Adelaide, Australia, *J. Atmos. Sci., 44*, 748-760.

Wang, L., M. A. Geller, and M. J. Alexander (2005), Spatial and temporal variations of gravity wave parameters. Part I: intrinsic frequency, wavelength, and vertical propagation direction, *J. Atmos. Sci., 62*, 125-142.

Warner, C. D.,and M. E. McIntyre (1999), Toward an ultra-simple spectral gravity wave parameterization for general circulation models, *Earth Planets Space, 51*, 475-484.

Warner, C. D. and M. E. McIntyre, An ultra-simple spectral parameterization for non-orographic gravity waves, *J. Atmos. Sci., 58*, 1837-1857, 2001.

Watanabe S., Constraints on a non-orographic gravity wave drag parameterization using a gravity wave resolving general circulation model, *Sci. Online Lett. Atmos., 4*, 61-64.

Wu, D. L. and J. W. Waters (1997), Observations of gravity waves with the UARS Microwave Limb Sounder, in *Gravity Wave Processes and Their Parametrization in Global Climate Models*, edited by K. Hamilton, Springer Verlag, New York.

Wu, D. L. and F. Zhang (2004), A study of mesoscale gravity waves over the North Atlantic with satellite observations and a mesoscale model, J. Geophys. Res, 109, D22104, doi:10.1029/2004JD005090.

Wu, D. L., P. Preusse, S. D. Eckermann, J. H. Jiang, M. de la Torre Juarez, L. Coy, B. Lawrence, and D. Y. Wang (2006), Remote sounding of atmospheric gravity waves with satellite limb and nadir techniques, *Adv. Space Res., 37*, 2269-2277.

Wu, D. L., and S. D. Eckermann (2008), Global gravity wave variances from Aura MLS: Characteristics and interpretation, *J. Atmos. Sci.*, in press.

Wüst S. and M. Bittner (2006), Non-linear resonant wave-wave interaction (triad): Case studies based on rocket data and first application to satellite data, *J. Atmos. Sol. Terr. Phys., 68*, 959-976.

Yee, J. H., E. R. Talaat, A. B. Christensen, T. L. Killeen, J. M. Russell, and T. N. Woods (2003), TIMED instruments, *Johns Hopkins APL Technical Digest 24 (2)*, 156-164.

Figure 1. Launch distribution of one SCE (λ_h =200 km, c =30 ms^{-1}, $\hat{u}_l$ =1 ms^{-1}). At each black asterisk eight rays are launched in eight different directions. Rays starting from 0° longitude are shown as an example. Color code gives altitude along ray trajectories. The '+' shows the location where the ray is terminated.

Figure 2. Comparison of July SABER GW squared amplitudes with zonal mean winds and different GROGRAT SCEs as specified in Table 1. Panel a) shows the zonal mean zonal wind composed from ECMWF and TIME-GCM, Panel b shows average July GW squared amplitudes deduced from SABER tempearature measurements. GROGRAT results for mesoscale waves with 200 km horizontal wavelength are shown in panels c)-g) and results for long horizontal wavelength GWs are show in panels h) and i). Temperature squared amplitudes are plotted in dezibel relative to 1 K^2, i.e. using alogarithmic color scale. For details see text.

Figure 3. Comparison of July SABER GW squared amplitudes with zonal mean zonal winds and results from different GROGRAT composite experiments. Panels a and b are the same as in Figure 2. The composite experiments (panels c - g) differ in the intermittency factors used to weight different SCEs (cf. Table 1). For instance, the experiments shown in panels e - g include more fast, medium horizontal wavelength GWs than Exp. 00 and 04 (panels c and d). Temperature squared amplitudes are plotted in dezibel relative to 1 K^2. For details see text.

Figure 4. Comparison of measured absolute values of GW momentum flux by CRISTA-2 (Aug. 1997, panel a) and CRISTA-1 (Nov. 1994, panel e) with absolute values of momentum flux for Exp. 32 (b, f), 132 (c, g) and 232 (d, h) calculated for the 15 Aug. 2003 (b-d) and 15 Nov. 2003 (f-h). Horizontal dashed lines in the GROGRAT simulations indicate the altitude range of the CRISTA results. The three composites differ in the launch distribution of horizontal wavelengths. Exp. 32 uses λ_h =200 km for all mesoscale components, Exp. 132 λ_h =200 km for the fast waves and λ_h =500 km for the slow waves dominating the lower altitudes, and Exp. 232 uses λ_h =500 km for all mesoscale components. For discussion see text.

Figure 5. Global maps of SABER GW squared amplitudes for vertical wavelengths from 5 km to 50 km at 28 km altitude. Values are binned according to calendar month for the time period from February 2002 to December 2006.

Figure 6. Global maps for 28 km altitude of GROGRAT GW squared temperature amplitudes from composite Exp232 for vertical wavelengths from 5 km to 50 km. For details see text.

Figure 7. Same as Figure 5c, but for altitudes of 40, 50, 60, and 70 km

Figure 8. Same as Figure 6, but for July and altitudes of 40, 50, 60, and 70 km

Figure 9. Time series of zonal mean GW squared amplitudes. SABER values (left column) are monthly averages combining data from 2002 to 2006, GROGRAT values from Exp. 232 (right column) are calculated from every third day of each month in 2003 and 2004. Color scales are the same for SABER and GROGRAT results for the respective altitudes of 30 km, 40 km, 70 km and 95 km. See text for further discussion.

Figure 10. Time series of SCEs 4, 8, 16, 22, 23 and 18 at 80 km (columns A, C) and 95 km (columns B, D) altitude. The reversal from summer minimum to summer maximum between 80 and 95 km altitude is observed only in the fast mesoscale SCEs.

Figure 11. Time series of zonal momentum flux for composite 232 at 70 km altitude. Color code gives the absolute value of zonal GW momentum flux given in dezibel over 1 Pa, contour lines show direction: solid contours indicate positive values, i.e. preferentially eastward propagation, dashed contours negative values, i.e. preferentially westward propagation.

Figure 12. Zonal mean GW induced forcing for 15 July 2003 from GROGRAT for composite Exp232. Left column (panels a, c, e) shows zonal acceleration, right column (panels b, d, f) shows meridional acceleration. The uppermost row (a, b) gives the total values, the middle row (c, d) the acceleration due to horizontal refraction of the wave vector, and the lowermost row (e, f) shows the relative contribution that is attributed to horizontal refraction, i.e. panels e and f give the percentual contribution of panels c and d to the total forcing shown in panels a and b.

Figure 13. Zonal means of the latitude difference between the launch location and the point of observation. Model results for composite 232 are shown for 15 July 2003. Panel a shows the average weighted only by the intermittency factors also used for the squared amplitudes and momentum flux values; panel b is additionally weighted by the absolute value of momentum flux of the individual waves; panel c and d are additionally weighted by the acceleration in the zonal and meridional direction.

Table 1. Overview of the launch parameters for all SCEs considered in the paper. The panel is given for those SCEs shown in Figure 2. The different composites (Ex0, ... Ex232) shown in Figure 3 differ in the intermittency factor (IMF) attributed to the single SCEs in generating the composite.

SCE #	Fig.	λ_h [km]	c_h [ms^{-1}]	ampl. $\hat{u}_l$ [ms^{-1}]	Ex00 IMF	Ex04 IMF	Ex14 IMF	Ex32 IMF	Ex132 IMF	Ex232 IMF
BGRD				0.5 K	5.0	5.0	5	0	0	0
1	2c	200	3	6.00	1.0	1.0	10	20	0	0
2		500	3	6.00	0.0	0.0	0	0	20	20
3		200	10	20.00	0.4	0.4	10	5	0	0
4		500	10	20.00	0.0	0.0	0	0	5	5
5		200	20	2.00	0.0	0.0	5	5	0	0
6		500	20	2.00	0.0	0.0	0	0	5	5
7	2d	200	30	1.00	1.0	0.0	2	5	0	0
8		500	30	1.00	0.0	0.0	0	0	5	5
9	2e	200	31	0.20	0.0	1.0	10	10	10	0
10		500	31	0.20	0.0	0.0	0	0	0	10
11		200	40	0.10	0.0	0.0	10	20	20	0
12		500	40	0.10	0.0	0.0	0	0	0	20
13	2f	200	50	0.20	0.5	0.0	2	0	0	0
14		500	50	0.20	0.0	0.0	0	0	0	0
15	2g	200	51	0.05	0.0	0.5	30	50	50	0
16		500	51	0.05	0.0	0.0	0	0	0	50
17		200	90	0.05	0.0	0.0	0	60	60	0
18		500	90	0.05	0.0	0.0	0	0	0	60
19		2000	15	2.00	0.0	0.0	0	30	30	30
20		1000	30	1.00	0.0	0.0	0	0	0	0
21		1500	30	1.00	0.0	0.0	20	20	20	20
22		2000	60	0.20	0.0	0.0	30	20	20	20
23	2h	2000	61	0.05	0.0	0.0	40	60	60	60
24		2000	30	1.00	1.0	1.0	20	20	20	20
25	2i	3000	30	6.00	1.0	1.0	20	5	5	5
26		6000	30	30.00	2.0	1.0	40	0	0	0

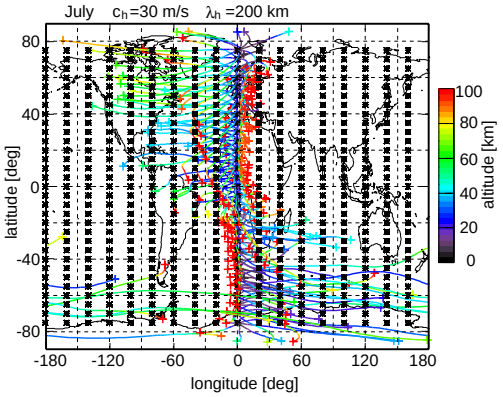

Figure 1. Launch distribution of one SCE (λ_h =200 km, c =30 ms^{-1}, $\hat{u}_l$ =1 ms^{-1}). At each black asterisk eight rays are launched in eight different directions. Rays starting from 0° longitude are shown as an example. Color code gives altitude along ray trajectories. The '+' shows the location where the ray is terminated.

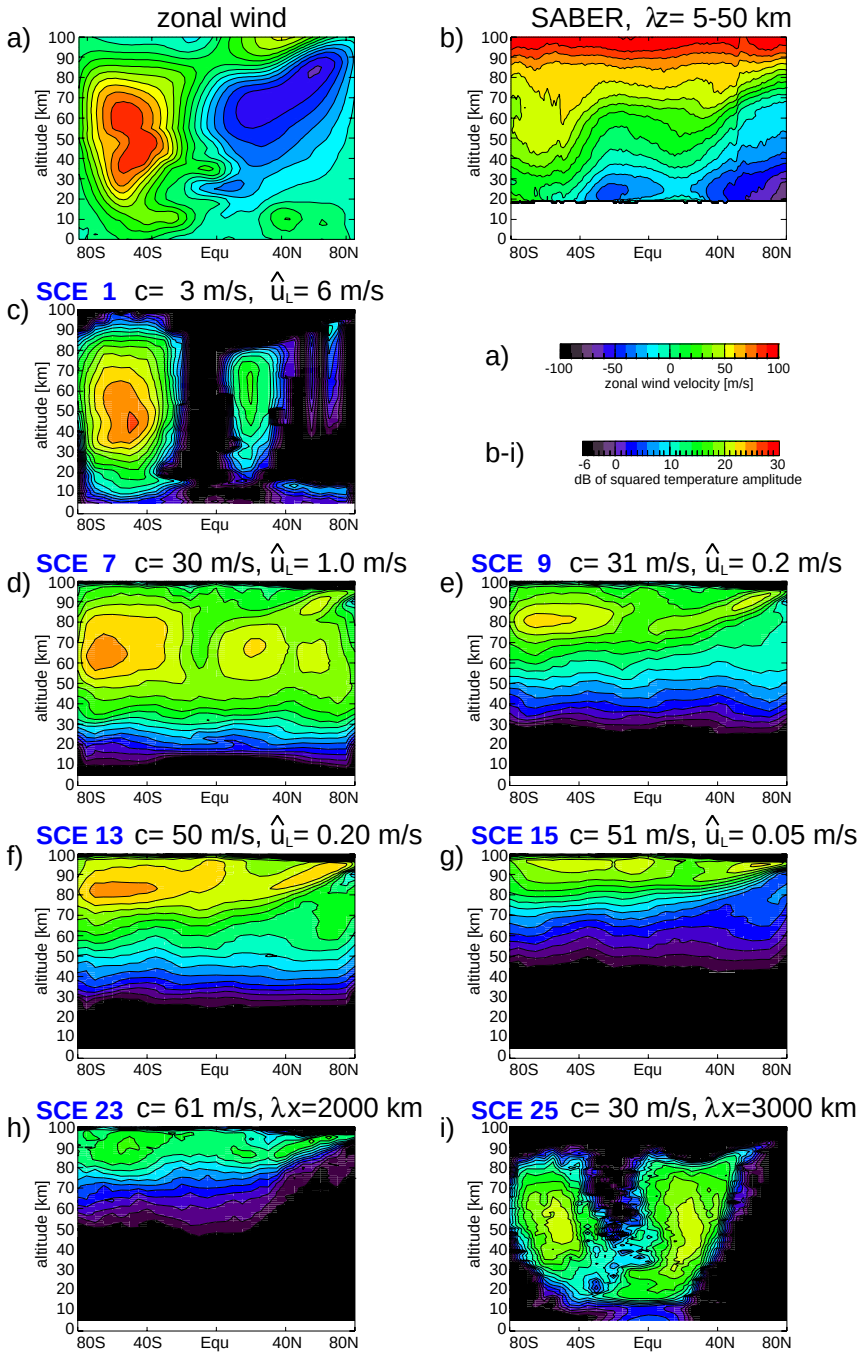

Figure 2. Comparison of July SABER GW squared amplitudes with zonal mean winds and different GROGRAT SCEs as specified in Table 1. Panel a) shows the zonal mean zonal wind composed from ECMWF and TIME-GCM, Panel b shows average July GW squared amplitudes deduced from SABER tempearature measurements. GROGRAT results for mesoscale waves with 200 km horizontal wavelength are shown in panels c) - g) and results for long horizontal wavelength GWs are show in panels h) and i). Temperature squared amplitudes are plotted in dezibel relative to 1 K^2, i.e. using alogarithmic color scale. For details see text.

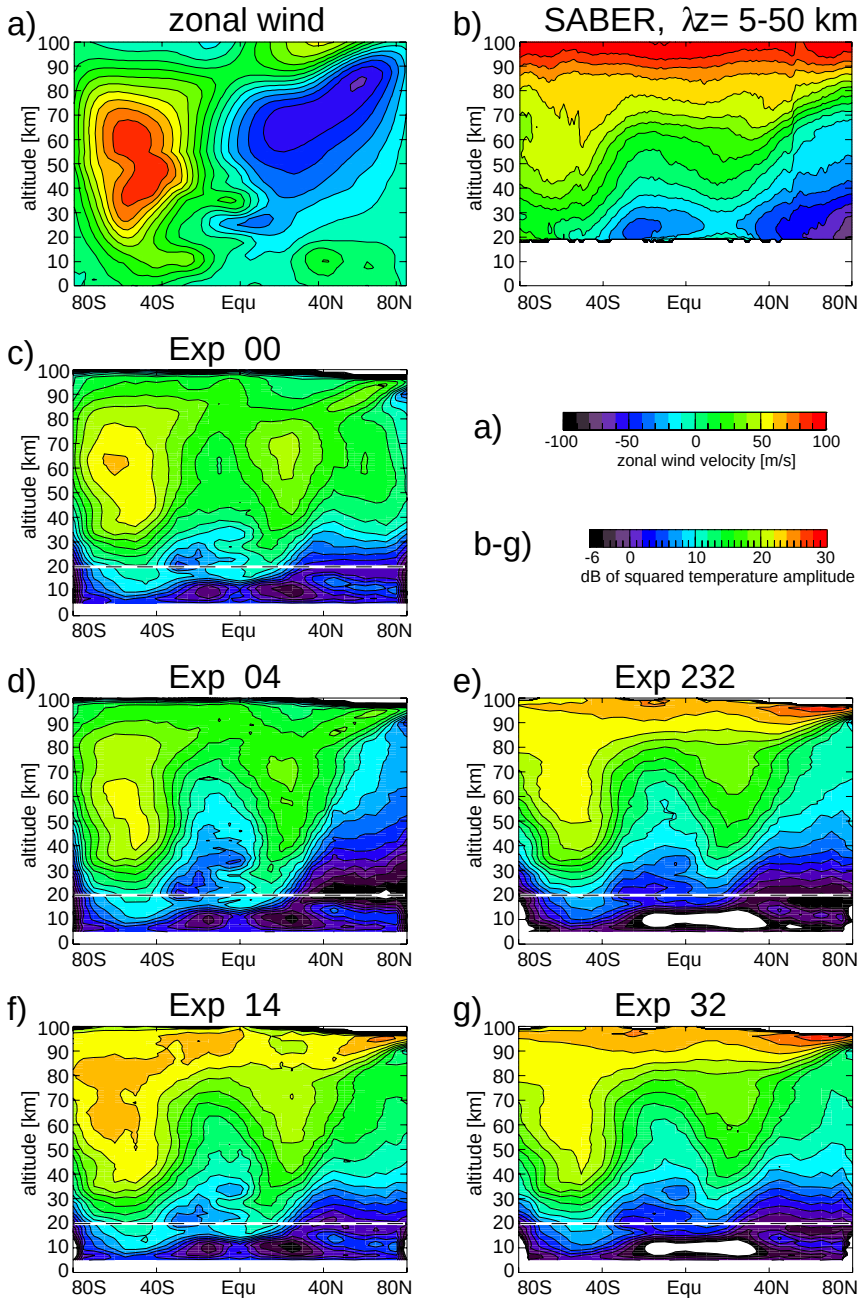

Figure 3. Comparison of July SABER GW squared amplitudes with zonal mean zonal winds and results from different GROGRAT composite experiments. Panels a and b are the same as in Figure 2. The composite experiments (panels c - g) differ in the intermittency factors used to weight different SCEs (cf. Table 1). For instance, the experiments shown in panels e - g include more fast, medium horizontal wavelength GWs than Exp. 00 and 04 (panels c and d). Temperature squared amplitudes are plotted in dezibel relative to 1 K^2. For details see text.

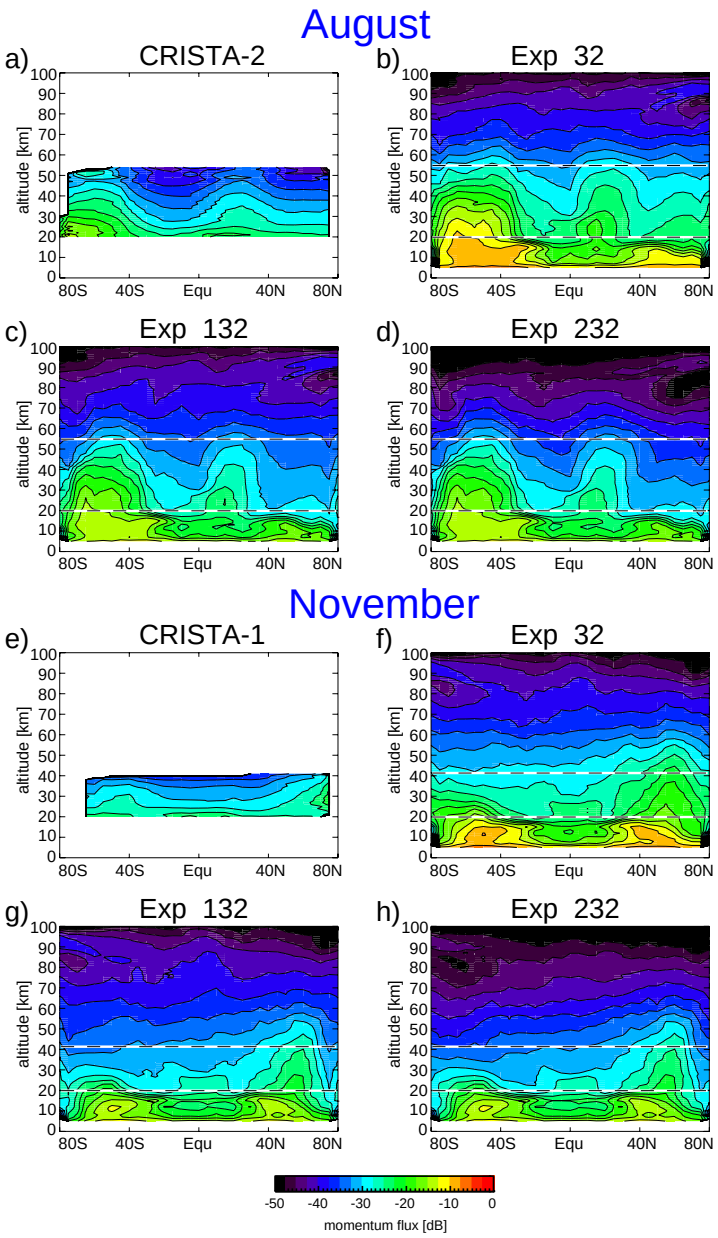

Figure 4. Comparison of measured absolute values of GW momentum flux by CRISTA-2 (Aug. 1997, panel a) and CRISTA-1 (Nov. 1994, panel e) with absolute values of momentum flux for Exp. 32 (b, f), 132 (c, g) and 232 (d, h) calculated for the 15 Aug. 2003 (b-d) and 15 Nov. 2003 (f-h). Horizontal dashed lines in the GROGRAT simulations indicate the altitude range of the CRISTA results. The three composites differ in the launch distribution of horizontal wavelengths. Exp. 32 uses λ_h =200 km for all mesoscale components, Exp. 132 λ_h =200 km for the fast waves and λ_h =500 km for the slow waves dominating the lower altitudes, and Exp. 232 uses λ_h =500 km for all mesoscale components. For discussion see text.

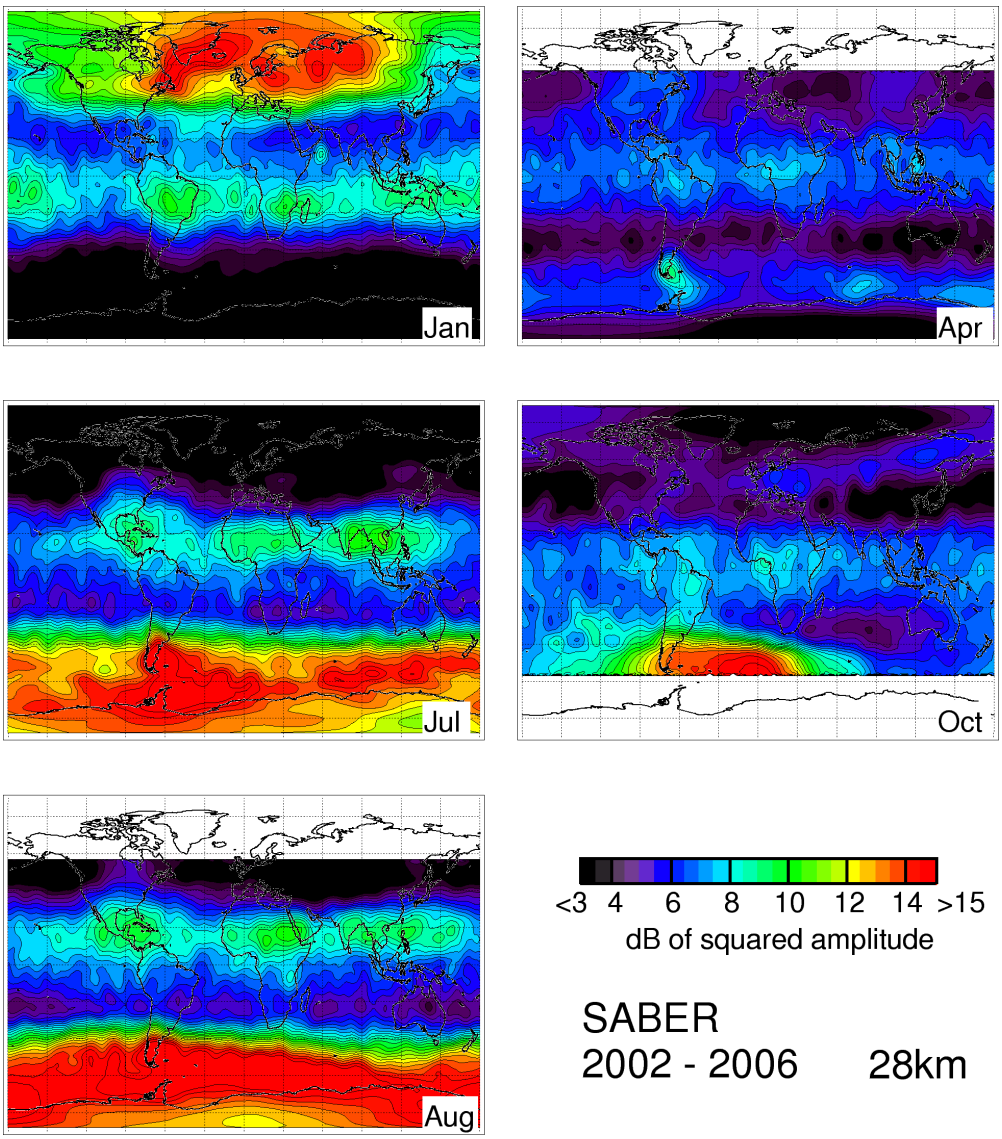

Figure 5. Global maps of SABER GW squared amplitudes for vertical wavelengths from 5 km to 50 km at 28 km altitude. Values are binned according to calendar month for the time period from February 2002 to December 2006.

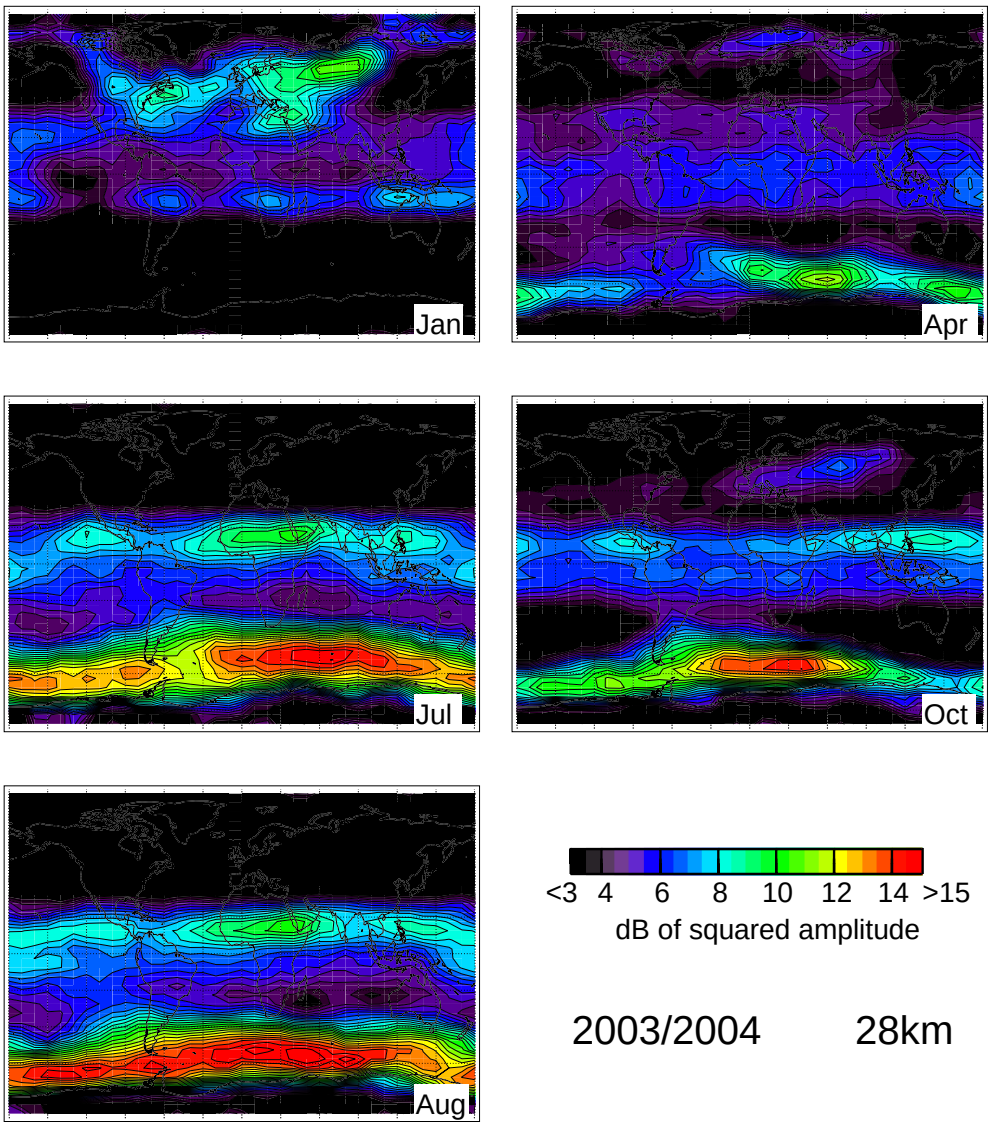

Figure 6. Global maps for 28 km altitude of GROGRAT GW squared temperature amplitudes from composite Exp232 for vertical wavelengths from 5 km to 50 km. For details see text.

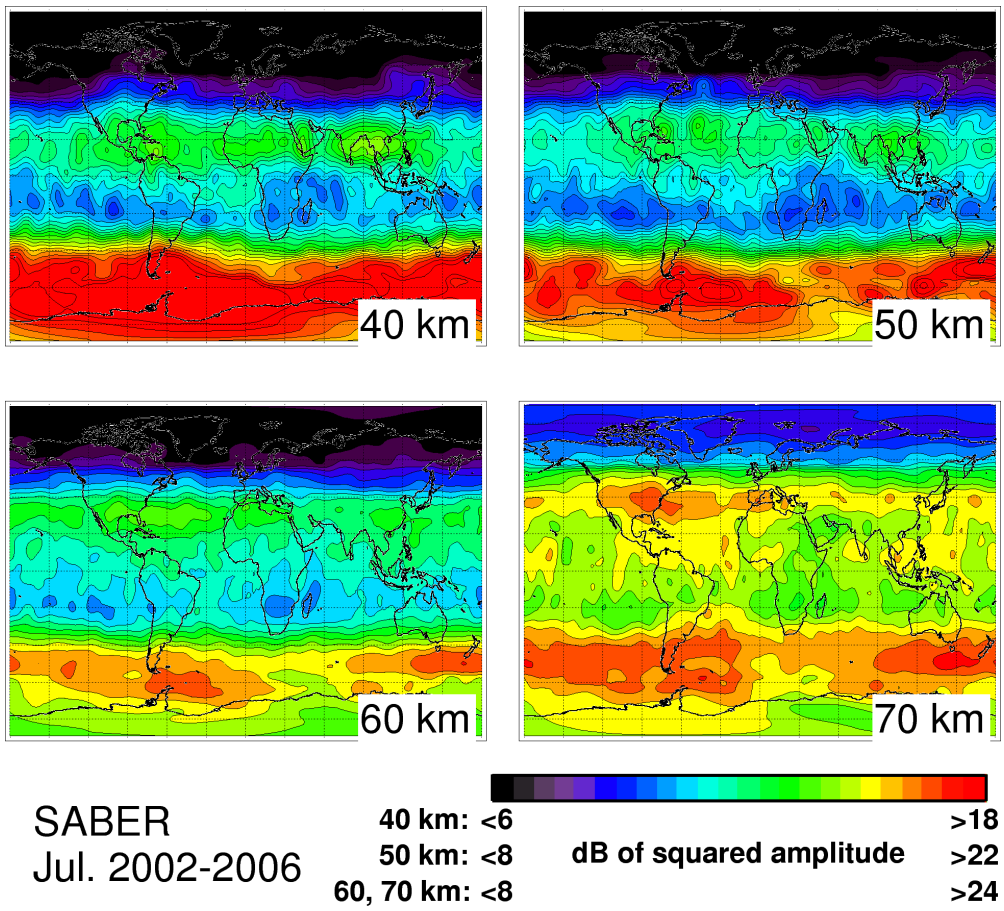

Figure 7. Same as Figure 5c, but for altitudes of 40, 50, 60, and 70 km

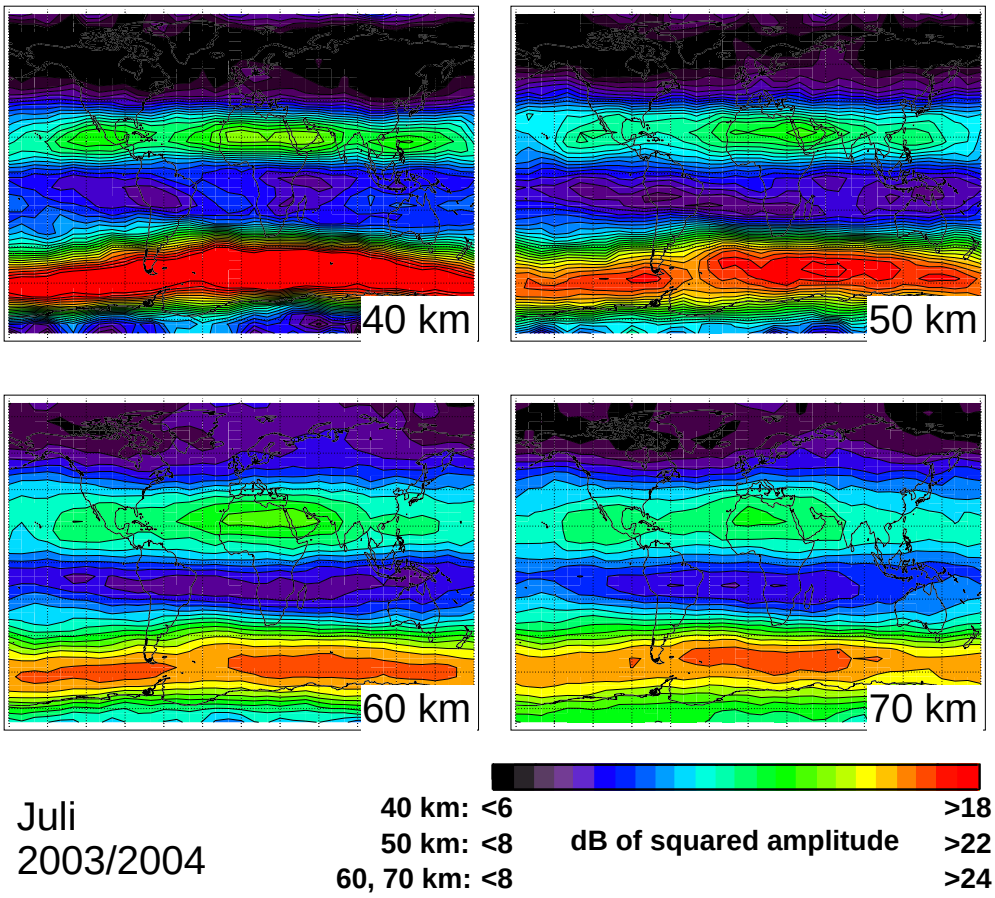

Figure 8. Same as Figure 6, but for July and altitudes of 40, 50, 60, and 70 km

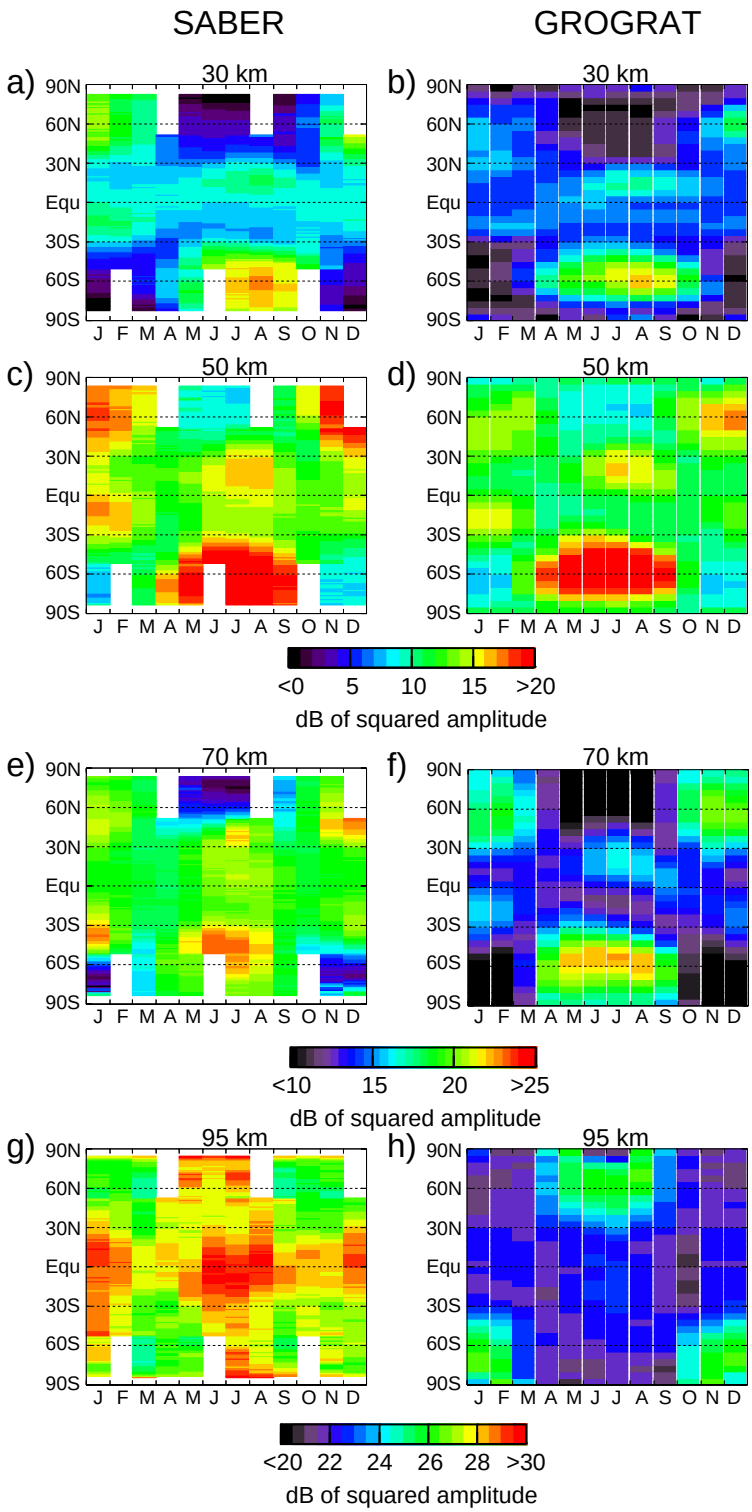

Figure 9. Time series of zonal mean GW squared amplitudes. SABER values (left column) are monthly averages combining data from 2002 to 2006, GROGRAT values from Exp. 232 (right column) are calculated from every third day of each month in 2003 and 2004. Color scales are the same for SABER and GROGRAT results for the respective altitudes of 30 km, 40 km, 70 km and 95 km. See text for further discussion.

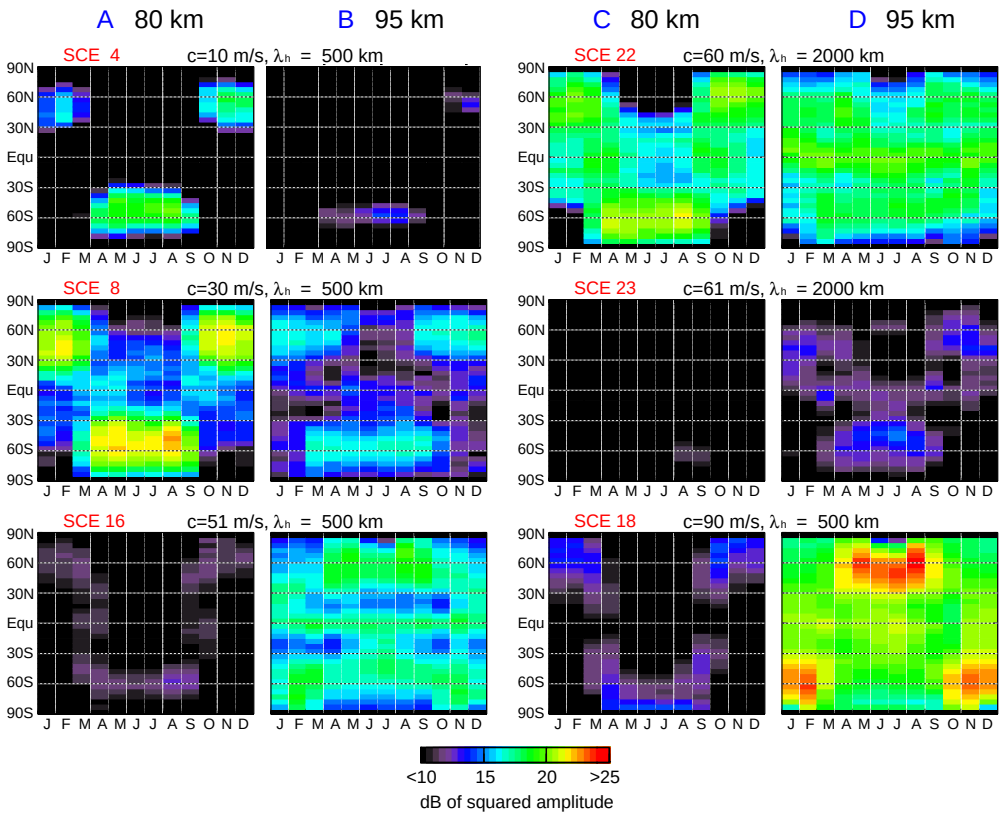

Figure 10. Time series of SCEs 4, 8, 16, 22, 23 and 18 at 80 km (columns A, C) and 95 km (columns B, D) altitude. The reversal from summer minimum to summer maximum between 80 and 95 km altitude is observed only in the fast mesoscale SCEs.

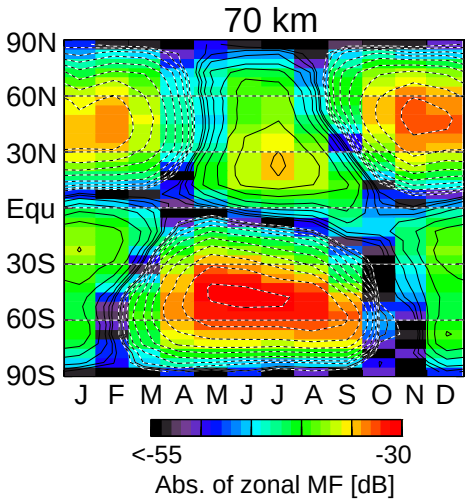

Figure 11. Time series of zonal momentum flux for composite 232 at 70 km altitude. Color code gives the absolute value of zonal GW momentum flux given in dezibel over 1 Pa, contour lines show direction: solid contours indicate positive values, i.e. preferentially eastward propagation, dashed contours negative values, i.e. preferentially westward propagation.

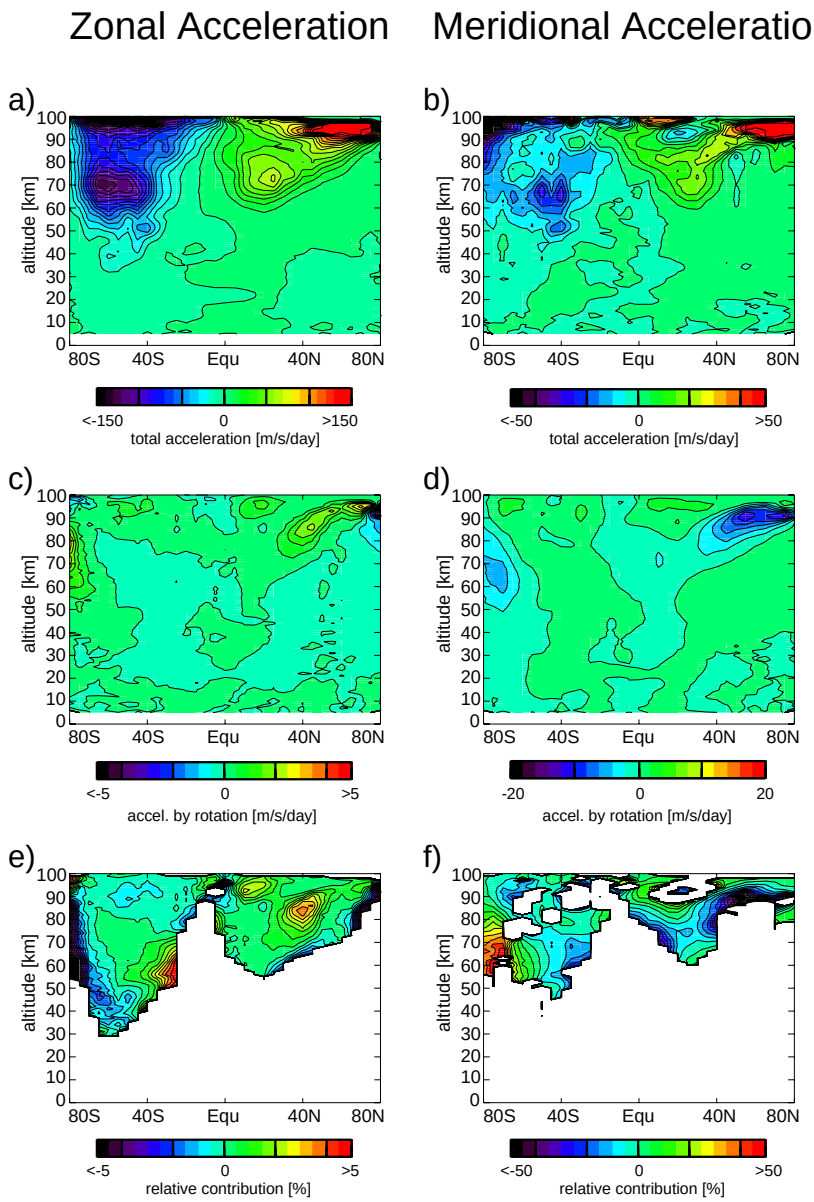

Figure 12. Zonal mean GW induced forcing for 15 July 2003 from GROGRAT for composite Exp232. Left column (panels a, c, e) shows zonal acceleration, right column (panels b, d, f) shows meridional acceleration. The uppermost row (a, b) gives the total values, the middle row (c, d) the acceleration due to horizontal refraction of the wave vector, and the lowermost row (e, f) shows the relative contribution that is attributed to horizontal refraction, i.e. panels e and f give the percentual contribution of panels c and d to the total forcing shown in panels a and b.

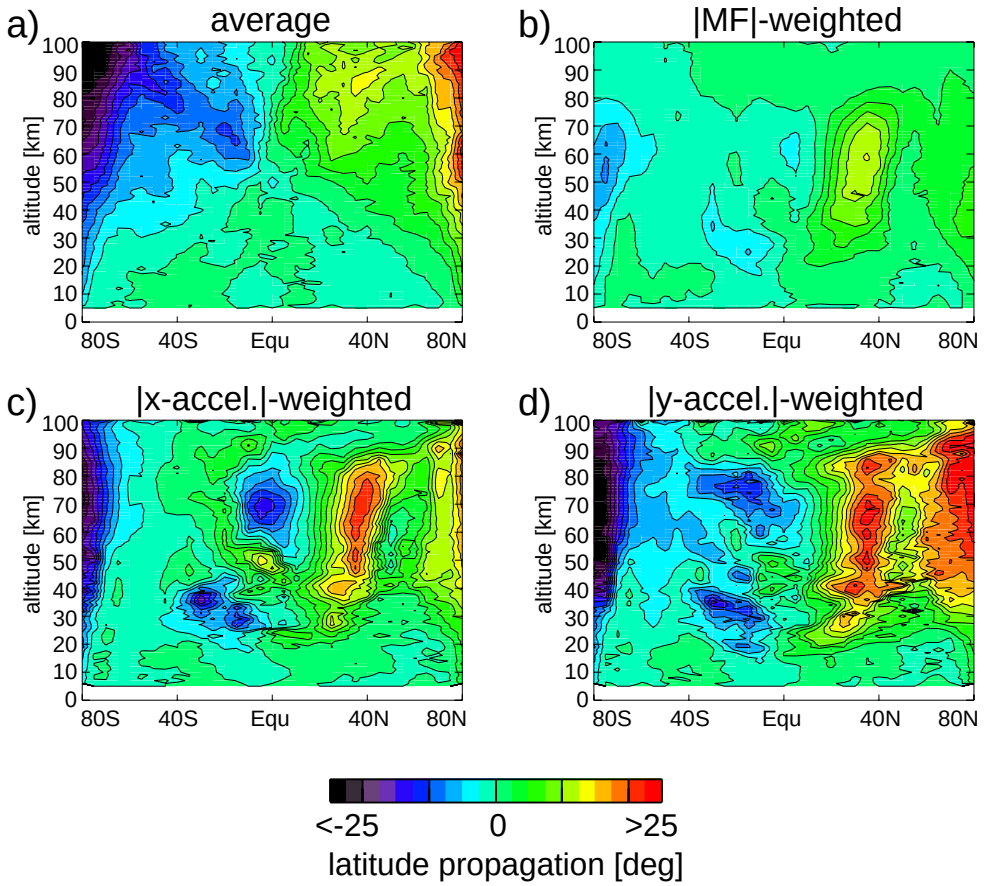

Figure 13. Zonal means of the latitude difference between the launch location and the point of observation. Model results for composite 232 are shown for 15 July 2003. Panel a shows the average weighted only by the intermittency factors also used for the squared amplitudes and momentum flux values; panel b is additionally weighted by the absolute value of momentum flux of the individual waves; panel c and d are additionally weighted by the acceleration in the zonal and meridional direction.